Effect of water flow and chemical environment on microbiota growth and composition in the human colon

Jonas Cremer*, Markus Arnoldini*, Terence Hwa

Supplementary Information

Supplementary Text

In this supplementary text we give detailed information on experimental methods and how we derived model parameters based on literature data on human physiology. We also present the details of the mathematical model. Cross-references within this document are denoted by 'SI section-number'. Supplementary Figures and Tables are referred to as 'S' followed by the figure or table number. Tables in this document not mentioned in the main-text are labeled alphabetically (Table A, B etc).

Definition of used terms:

- **SCFA:** Short chain fatty acids. With 'total SCFA' we refer to all acidic fermentation products. In particular, we also include lactic acid and succinic acid, strictly not belonging to the group of short chain fatty acids.
- **Colon:** Following its sloppy but frequent usage, we here use this term as a synonym for large intestine, i.e. we also include the cecum and rectum when using this term without referring to a specific region. With proximal colon, we mean the cecum and the ascending colon. With distal colon, we mean the remaining colon from the descending colon onwards.

1 Detailed Experimental Methods

In this supplementary section we give an overview on the used experimental methods and the model formulation. More details on modeling and parameter-estimations are given in the other, following sections of this supplementary text.

1.1 Bacterial strains and culture conditions

Bacteroides thetaiotaomicron (ATCC 29148) and *Eubacterium rectale* (ATCC 33656) were obtained from the American Type Culture Collection and stored at -80°C. To start a culture, frozen tubes were passed into an anaerobic chamber (Coy Laboratory Products) through an airlock, and seeding cultures were inoculated directly from freezer stocks. Cells were grown in 16mm glass tubes in a dry bath (Eppendorf ThermoMixer C with a 15ml Thermoblock) at 37°C shaking at 500rpm.

The medium for seeding cultures was Wilkins Chalgren Broth (WCB, Oxoid) for *Bacteroides thetaiotaomicron*, and TYG (based on (1)) for *Eubacterium rectale*. TYG medium is 1% Tryptone, 0.5% Yeast extract, 0.2% Glucose, 100mM K_2HPO_4/KH_2PO_4 (adjusted ratio for pH 7.2), 4.1mM Cysteine, 200µM Histidine, 6.8µM $CaCl_2$, 140nM $FeSO_4$, 81µM $MgSO_4$, 4.8mM $NaHCO_3$, 1.4mM $NaCl$, 1.9µM Hemin, and 5.8µM Menadione.

After growth in WCB and TYG, respectively, cultures from both strains were diluted to give precultures. The medium used contains 1% Tryptone, 20mM Glucose, 100mM K_2HPO_4/KH_2PO_4 (adjusted ratio for desired pH), 50mM $NaCl$, 0.5mM $CaCl_2$, 0.4mM $MgCl_2$, 50µM $MnCl_2$, 50µM $CoCl_2$, 4µM $FeSO_4$, 5mM Cysteine, 20mM $NaHCO_3$, 5mM Na_2SO_4, 20mM NH_4Cl, 1.2mg/l Hemin, 1mg/l Menadione, 2mg/l Folinic acid, and 2mg/l vitamin B12. For low pH values, HCl was added to the medium to reach the desired pH. See Supplementary Text 1.7 for discussion of growth conditions and typical luminal compositions bacteria encounter in the colon.

In exponential phase, OD at 600nm was determined, and the precultures were diluted to an OD of around 0.02 in the same medium they were growing in before. The OD at 600nm of these experimental cultures was then measured at regular intervals, by removing samples of 200µl from the cultures and transferring these samples to a semi-microcuvette (Starna Cells) in a spectrophotometer (Spectronic 20 Genesys, Spectronic Instruments). The samples were discarded after the measurements.

1.2 Metabolite analysis

For metabolite analysis, four samples of 200µl were taken at regular intervals during exponential growth, transferred to 0.22µm nylon filter centrifuge tubes (Corning Costar Spin-X Centrifuge Tubes) and immediately filtered by centrifugation. 80µl of filtered sample was then transferred to HPLC sample tubes and analyzed using a Shimadzu Prominence HPLC using RID detection. The HPLC setup was as follows: isocratic HPLC was used with 10mM H_2SO_4 as mobile phase at 0.4ml/min pump speed; samples were kept at room temperature in the autosampler (Shimadzu SIL-10AF); 20µl of sample was injected; samples were separated using ion exchange chromatography; the column (Phenomenex, Rezex ROA-Organic Acid H+ (8%), LC column 300 x 7.8mm) that was kept in a column oven (Shimadzu STO-20A) at 40°C; data from the RID detector (Shimadzu RID-20A) was recorded for 40min. Data was subsequently exported and analyzed in R (2). In short, peaks of interest were isolated, a baseline correction (based on the Sensitive Nonlinear Iterative Peak clipping algorithm, using the function spectrumBackground) was applied using the R package Peaks (3). Gaussian functions were then fit to the corrected data, and the area under the fit curves was calculated. The concentrations corresponding to given areas under peaks were determined by running standards with known concentrations of the compounds of interest.

2 Physiology and flow dynamics of the human colon

2.1 Dimensions of the colon

Measurements of lengths and volumes/diameters of different parts of the large intestine have been performed by a number of different methods, ranging from measurements at autopsy (6, 7), interoperative measurements (8), CT colonoscopy (9), MRT or radiological measurements (10, 11). The different studies report comparable average lengths with a strong variation between individuals. For example, variation between 120 and 250cm in a study with 505 adults has been reported (9). Here, we use the numbers stated by (6). Numbers used for the model are presented in Table A.

Diameters of the different parts of the colon have been measured mainly by autopsy and CT studies, and outer diameters of the colon were reported. However, for bacterial growth dynamics in the colon, the inner diameter (i.e., the diameter of the luminal tube) is important. To obtain an estimate for the inner diameter, we use MRT data on luminal volumes (11) of the colon to calculate the luminal diameter. MRT measurements of the undisturbed colon report the total volume of part of the colon (ascending, transverse and descending colon) to be around 550ml. Measurements of transition times through the emptied colon estimate a total volume of 300ml for the total colon. We assume these reported values to be an upper and lower bound for the total luminal volume of the colon, respectively: Pritchard et al (11) estimated luminal volumes of the full colon, whereas Devroede and Phillips (12) measured the luminal volume of the empty colon.

As Villi and folds are mostly absent in the colon, with crypts covered by the mucus layer, we then estimate the luminal surface to volume ratio by assuming a pipe-like luminal tube and calculate the corresponding luminal diameter. To calculate volumes and diameters of all of the colon segments, we assume the luminal diameter for the cecum to be comparable to the derived diameter for the ascending colon, and the luminal diameter of the sigmoid colon to be comparable with the diameter derived for the descending colon. Taking the reported volumes of different parts of the colon as measured by MRT (11), and their lengths (6), the estimated diameters (using upper volume boundaries) range between 2.1 and 3.3 cm (see Table B). This upper bound estimation corresponds to a total luminal volume of approximately 950ml. To estimate lower bounds of the luminal tube diameters in different parts of the colon, we assume a ratio of volumes in the different parts of the colon equal to what was observed by Pritchard et al (11) with the MRT measurements, but adding up to a total volume of 300ml, as observed by Devroede and Phillips (12). The resulting lower bound diameter estimation lies between 1.2 and 1.8 cm (see Table B).

Table A Anatomical dimensions of the large intestine. Published average anatomical dimensions and luminal volumes of the colon used in this study. Length and anatomical diameters from (Khashab et al. 2009) obtained by CT measurements. Luminal volumes from MRI measurements, see text.

	Length (cm)	Anatomical diameter (cm)	Volume (ml)
Cecum	6.7	7.6	
Ascending colon	23.1	6.1	203
Transverse colon	58.3	5.0	199

Descending colon	33.0	3.8	159
Sigmoid colon	49.0	3.5	
Rectum	19.5	6.5	
Total colon	189.5		

Table B Volume and diameter approximations of the luminal tube in different parts of the colon. Derived luminal diameter calculated assuming pipe shape, upper boundary by MRI measurements, lower bound by transient time measurements in the empty colon, see text. For the total colon, weighted averages are shown. Diameters in cm, volume in ml.

	Derived diameter of lumen tube, upper bound (MRT)	Assumed diameter, upper bound (MRT)	Derived Volume, upper bound (MRT)	Derived diameter, lower bound	Used
Cecum		3.3	57	1.8	2.6
Ascending colon	3.3	3.3	198	1.8	2.6
Transverse colon	2.1	2.1	202	1.2	1.8
Descending colon	2.5	2.5	162	1.4	1.8
Sigmoid colon		2.5	240	1.4	1.8
Rectum		2.5	95	1.4	1.8
Total colon (aver.)		2.5	955		1.95

For the estimation of flow velocities, we use the means of the upper bound and lower bound estimations, and distinguish between a larger diameter (cecum and ascending colon with a diameter of $2.6\ cm$) and a smaller diameter (transverse, descending and sigmoid colon as well as rectum with a diameter of $1.8\ cm$). This keeps the geometry simple but takes into account that cross-sections change by up to a factor of 2 from the ascending to the transverse colon (in the model, cross-section is changing from $5.3\ cm^2$ to $2.5\ cm^2$). For the simulations, we use $d_{col} = 1.95cm$ as constant luminal diameter.

2.2 Flow dynamics and water absorption in the large intestine

To estimate flow-velocity profiles along the different parts of the colon, let us first consider a scenario without water absorption through the epithelial layer. Inflow into the colon from the ileum has been measured (13, 14) to be approximately $Q_{il} = 1.5\ l \cdot day^{-1}$. Of this volume, not more than $150\ ml \cdot day^{-1}$ ends up as fecal output, with fecal weights mostly below $100\ g \cdot day^{-1}$: $Q_{fec} \approx 0.1\ l \cdot day^{-1}$ (15, 16). If we first assume that the average flow-velocity is set by the daily inflow from the ileum ($Q_{il} = 1.5\ l \cdot day^{-1} \approx 1\ ml \cdot \mathrm{min}^{-1}$) and the cross-sections at different parts of the colon (as discussed before, see SI 2.1, Table B), the flow-velocities would vary between $32\ \mu m \cdot s^{-1}$ (proximal colon with larger diameter) and $67\mu \cdot s^{-1}$ (distal colon with smaller diameter). In a second scenario, assume the flow would match the outflow rate from the rectum ($Q_{fec} \approx 0.1\ l \cdot day^{-1}$). Using the same diameters, the velocity would be as low as $5\ \mu m \cdot s^{-1}$ or even lower. The real flow velocity profile lies between these two values and depends on water absorption by the colonic epithelium: More than 90% of the water

entering the colon from the ileum is absorbed in the colon, and water absorption is considered as one major function of the colon (6, 17, 18). Through this decrease in luminal water content, the net flow velocity is decreasing strongly towards the rectum.

To estimate the true flow velocities along different parts of the colon, one has to estimate the change of net water absorbance along the colon: Water absorbance has been shown to vary along the colon, with stronger absorbance in the proximal colon, in particular the cecum and ascending colon (13, 17, 19). There is no water-absorbance in the rectal part of the colon (20). Measurements with physiological solutions containing non-absorbable markers infused at the cecum at high flow rates (e.g. 10ml/min) show that the maximal capacity for water absorption rate in the colon is approximately 2ml/min, or approximately 3 l/day (6, 17, 20), roughly twice as much as the typical daily volume coming from the ileum. Taking this as an upper bound for water absorption by the whole colon, and assuming a homogenous distribution of water absorption along the epithelial surface of the colon (excluding the rectum), one ends up at different maximum absorption rates per length in different parts of the colon, see Table Table C. Given these reported rates of water absorption, most of the water is expected to be already absorbed at the distal end of the transverse colon.

Table C Approximated water absorption and resulting veolocity profile along the colon. Calculations based on measured maximum water absorption in colon, and water absorption along most of the colon. See text for details of deviation.

	Surface (cm^2)	Fract. Surface	Water absorption rate, max ($ml\,min^{-1}\cdot cm^{-1}$)	Velocity gradient, max ($\mu m\,s^{-1}\cdot cm^{-1}$)
Cecum+Asc. Colon	243	24%	0.016	-0.52
Transv.+Desc.+Sigm	793	76%	0.011	-0.74
Total colon w/o rect.	1036	100%	0.012	

As a first approximation of the flow-profile, we assume an inflow rate of Q_{il}, and maximum apsorption along the ascending and transverse colon until the observed outflow-rate, Q_{fec}, has been reached. The corresponding flow-profile is shown in Figure S10, red line.

Studies indicate that absorption in the ascending colon might be stronger (17, 19). Thus the red line in Figure S10 is rather an upper limit of the real velocity profile in the proximal colon. While these studies indicate that there are possible differences, they also suggest that water-absorption is not varying very strongly between proximal and distal colon. A gradient more than 2x stronger seems to be unlikely. We thus take a 2x steeper profile as a lower boundary for the real flow velocity profile in the proximal colon. Flow velocities are expected to be in the range between upper and lower boundary (Figure S10, shaded blue area). As standard condition for simulations we use the average of both limits (Figure S10, blue line, and velocity panel in Figure 2):

$$v(x) = \begin{cases} v_{in} - v' \cdot x \; for \; x < \dfrac{v_{in} - v_{out}}{v'} \\ v_{out} \qquad\qquad else \end{cases} \tag{1}$$

with $v_{in} = 32\ \mu m/s$, $v_{out} = 5\mu m/s$ and $v' = 0.75\ \mu m/s \cdot cm^{-1}$. With this, the mean velocity in the proximal colon is given by $\overline{v_p} = 18.5\ \mu m \cdot s^{-1}$, with the upper and lower limits given by $\overline{v_p^+} = 24\ \mu m \cdot s^{-1}$ and $\overline{v_p^-} = 16.5\ \mu m \cdot s^{-1}$.

Using this velocity profile, the average transit time through the proximal colon is approximately $4.1\ h$, based on flow alone (without considering mixing), and it takes about $72\ h$ to pass through the whole colon.

Transit times through the ascending colon have been measured by following the movement of radiolabeled species through the intestine: For the undisturbed colon, an average time of 4.1 hours has been reported the passing of radiolabeled particles through the ascending colon (21). Reported transit times through the total colon are highly variable (reported values between 24 hours and more than 4 days). For example, Cummings et al report (22) average transit times for the whole gut to be 58 hours. Hammer and Phillips (23) report that it takes 34-48 for first radioactive test particle to appear in feces, with much longer average transit times (23) Our derived values for water absorption and velocity profiles are therefore in good agreement with reported literature values on passing times and water absorption.

2.3 Maintaining bacterial densities under high luminal flow

With the high fluid loads entering the colon ($\approx 1.5\ l/day$), mechanisms must be in place to counter-act a rapid depletion of cells being carried away by the strong flow. Understanding this mechanism is crucial for developing a quantitative model of bacterial growth dynamics. In this section, we discuss different possible mechanisms that might allow stable bacterial densities to persist in the presence of such a flow.

One possible mechanism for maintaining a stable bacterial density in the proximal colon is the permanent replenishment of bacterial cells from the small intestine (ileum). However, bacterial densities in the small intestine are very low. In particular, it has been shown that luminal fluid exiting the ileum have very low bacterial counts (24). In addition, bacterial compositions in the ileum and proximal colon are very different, with mostly facultative anaerobes in the ileum (24, 25) while obligate anaerobes dominate in the proximal colon.

Active motility of bacteria against the luminal flow is another possible mechanism to counteract flow. However, bacterial motility alone cannot provide a compelling explanation for the maintenance of high bacterial densities. First, from a physical perspective, upstream motility against the high flow rates (up to more than 30 µm/s,) would require continuous and directed swimming of bacteria which is unrealistic. Second, many abundant members of the gut microbiota do not carry genes for flagella (e.g. *B. thetaiotaomicron*, *B. ovatus*, *F. prausnitzii* (26)). In addition, mass spectrometry analysis has shown that the structural flagella protein is not strongly expressed in the colon (27).

Yet another possible mechanism stabilizing the bacterial density in the lumen is the replenishment by bacteria shed from a reservoir like a biofilm adhering to the colonic walls (28-30). In our view, this “wall growth” is not sufficient for maintaining the high densities in the lumen either. First, the human proximal colon has an inner diameter of 20-30 mm, leading to an unfavorably small ratio of surface to volume: For realistic bacterial growth rates, a proper replenishment would require the number of wall-bound bacteria to be comparable to that of bacteria in the lumen, whereas the observed abundance of the wall-bound bacteria is several orders of magnitude lower (see detailed analysis in (5)). Second, the colonic epithelium is covered by a mucus layer, and bacterial densities in this mucus layer have been

reported to be low (31, 32). Third, most cells in the luminal bacterial community are strict anaerobes, and are not able to grow in the mucus layer where they are exposed to substantial oxygen levels due to the proximity to the aerobic epithelium (33, 34).

In conclusion, while all the mechanisms mentioned above might be important for certain aspects of gut ecology, they are insufficient to explain the high bacterial densities observed in the proximal colon. Instead, we argue that mixing by active wall contractions can account for the high densities. Frequent, uncorrelated contractions of the intestinal walls have been observed in the proximal colon (35, 36). These contractions generate hydrodynamic backflow, which drags a fraction of the luminal contents (including bacteria) against the main flow direction. This mixing has also been observed directly (23), and allows a quantification of its strength, as we show in SI 2.4. In combination with bacterial growth, this mixing helps to prevent depletion of bacteria from the colon, even for the large flow rates observed in the proximal colon: In SI 2.5, we provide a detailed analysis of the effect of mixing on bacterial growth dynamics. In brief, anticipating this analysis: Mixing can be estimated by an effective diffusion, $D \approx 10^6\ \mu m^2/s$. This mixing together with bacterial growth, $\lambda_0 \approx 1\ h^{-1}$, can overcome flow-velocities of up to $v_{washout} \approx \sqrt{D\lambda} \gtrsim 22\ \mu m/s$ which alone would lead to a washout of bacterial cells.

2.4 Quantifying mixing dynamics in the large intestine

To derive an estimate for the strength of mixing in the proximal colon, we focus on studies by Phillips and coworkers (12, 23). In particular, we analyze the results reported by Hammer and Phillips (23). The authors have followed the emerging spatial and temporal distributions of non-absorbable markers (radiolabeled fluid and particles) infused into the ceca of human subjects. To study the possible link between diarrhea and fluid load in the large intestine, the authors infused different volumes containing these markers into the cecum, and observed the change in distribution over time.

In the following analysis, we focus on their data reported for the proximal colon, where most bacterial growth occurs. Hammer and Phillips (23) tracked radiolabeled liquids and solids. In the following, we use the published results for liquids, but solids follow similar dynamics. Our analysis is based on observed numbers of mean times to exit the proximal colon, and the percentage of radioactive signal that has passed the ascending colon after 4 hours (data from Tables 4 and 5 in (23)). This data is plotted in Figures S9 A and B.

In order to derive a quantitative measure for the strength of mixing in the human gut from the data in Hammer and Phillips' study (Figures S9 A and B), we developed a phenomenological model: we model marker distributions and flow by convection-diffusion equations and describe mixing by effective diffusion. This simplified simulation approach has been shown to be useful in *in vitro* experiments to approximate mixing behavior by peristalsis-like wall contractions in a channel under constant flow(5). In the present simulations, we vary two parameters, flow velocity and diffusion. All simulations start with the introduction of a localized peak of marker at the beginning of the colon (Figure S9 C, purple line). Flow moves the peak forward, and mixing widens the distribution over time. As this distribution moves along the colon, the fraction that has passed the proximal colon increases (Figure S9 C, parts of the distributions left of the dashed black line. The change in this passed fraction over time therefore has a sigmoid shape, reaching from 0 to 100%. If we now change the flow velocity and the strength of mixing, we can simulate the dependence of the mean exit time (Figure S9 D) and of the fraction of marker that has passed the proximal colon after 4 hours (Figure S9 E) on these parameters. For mixing that is not too strong ($D < 200\ 10^4\ \mu m^2/s$), flow is the main factor driving the marker displacement towards the

distal colon, and the exit time increases strongly with lower flow velocities. This can be seen by the strong dependence of the mean exit times (Figure S9 D) and the passed fractions after 4h (Figure S9 E) on the flow velocity for low mixing. This changes for stronger mixing ($D > 200\ 10^4 \mu m^2/s$), where mixing is so strong that it can dominate the marker movement towards the distal colon; in this scenario, exit times do not decrease substantially, when flow rates decrease (Figure S9 D, light and dark blue lines). The passed fraction shows increasingly stronger deviations from the predicted sigmoid shape for stronger mixing (Figure S9 E); this can be rationalized by the fact that, for strong mixing, the bell-shaped distribution curve is so wide that the transport of marker is dominated by mixing rather than flow.

We can now compare the dynamics in our simulations with the observations by Hammer and Phillips. By doing so, we get reasonable upper and lower bounds for the mixing parameter. Measured mean exit times (Figure S9 A) rule out very strong mixing ($D > 200\ 10^4 \mu m^2/s$): the measured distribution of mean exit times clearly changes with the infused volume (and thus with flow velocity). This would not be the case if mixing was completely dominating the dynamics. $D = 200\ 10^4 \mu m^2/s$ thus gives us an upper bound for mixing. The measured passed fractions after 4 hours (Figure S9 B) rule out very weak mixing ($D < 50\ 10^4 \mu m^2/s$): for weak mixing, the very narrow peak of injected marker would only widen very little, and the passing of marker should be dominated by flow. One would thus expect a sharp transition from a 0% passed fraction after 4h for slower flow rates to a 100% passed fraction for higher flow rates. This behavior does not describe the experimental data; the measured passed fraction after 4h increases smoothly with increasing flow rates; when compared to simulation data, we can define a lower bound for mixing to be $D = 50\ 10^4 \mu m^2/s$. To directly compare simulations with observations we also plot mean exit time versus passed fraction after 4 hours (Figure S9 F). This allows comparison without the explicit relation between infused volume and flow-velocity. Again, the observed relation is only recovered for a diffusion in the range between 50 and $200\ 10^4 \mu m^2/s$.

Based on these estimations, we use $D = 100\ 10^4\ \mu m^2/s$ (orange lines in Figures S9 D-F) for our simulations if not indicated otherwise. For comparison, note that this is more than thousand times higher than native diffusion of smaller molecules like glucose in water.

2.5 Analysis of bacterial growth and washout

We now consider bacterial growth for the flow and mixing conditions that we have derived above (SI 2.2 and 2.4, respectively). We analyze how these parameters influence bacterial densities in an environment that has the geometry of the human colon, as derived in SI 2.1. What conditions have to be fulfilled to avoid a loss of all bacteria ("washout")?

In order to do this, we use a simplified version of our model that does not take pH feedback into account (i.e., $\phi(pH) = 1$), disregards SCFA and bicarbonate dynamics, and only considers one bacterial species (the full model is introduced in detail in SI 5). We assume a constant $pH = 7$ and a growth rate of $\lambda_0 = 1\ h^{-1}$. Yield is $Y = 0.1\ OD/mM$. Nutrient inflow is the same as for a standard Western diet, $N_{in} = 300\ mM \cdot day^{-1}$ (glucose equivalents, see SI 2.6).

We first make the simplifying assumption of a constant flow velocity along the whole length of the colon. For this scenario, the conditions where washout of bacteria from the colon occurs follow the analysis presented in (5): For strong mixing ($D \gtrsim 1000 \cdot 10^4\ \mu m^2/s$), the bacterial density dynamics resemble a well-mixed chemostat, with the washout condition given by a critical flow velocity $v_{CT}^* = \lambda \cdot L_S$. Here, L_S denotes the length of the system and λ denotes the bacterial growth rate. For high

velocities, $v > v^*_{CT}$, washout of bacteria occurs, while for smaller velocities, $v < v^*_{CT}$, a steady state solution with a stable bacterial population exists. Assuming the proximal colon is the growth zone, the system length is approximately given by $L_S = 0.3\,m$. For a typical growth rate, $\lambda_0 = 1.0\,h^{-1}$, the chemostat washout condition is thus approximately $v^*_{CT} \approx 80\,\mu m \cdot s^{-1}$. This number is much higher than the highest possible flow rate that we have derived in SI 2.2 ($v \approx 32\,\mu m \cdot s^{-1}$), and we can therefore safely assume that the chemostat washout condition is not fulfilled: for sufficiently strong mixing, bacterial washout is prevented in the human gut, and high bacterial densities are reached.

For weaker mixing, the system is not well mixed, and spatial profiles can form. The backflow against the average flow-direction is reduced and as a consequence, washout is more likely to occur. This can be described by an additional washout condition which is given by comparing the term for flow velocity that promotes a decrease in bacterial density with the two terms that promote higher bacterial densities, namely mixing and bacterial growth; this condition is approximately given by $\alpha \equiv \frac{v^2}{D\lambda_0} = 1.8$, see analysis in (5). This imposes a much stricter bound on the maximal flow velocity without washout. For the estimated mixing given by $D = 100 \cdot 10^4\,\mu m^2\,s^{-1}$ (see SI 2.4) and a fast growth rate, the critical velocity is given by approximately $v^*_\alpha \approx 22\,\mu m \cdot s^{-1}$.

In Figure S11, we show the changes in bacterial density (Figures S11 A-C) and nutrient concentrations (Figures S11 D-F) when changing the main parameters important to set washout, flow velocity (Figures S11 A and D), growth-rate (Figures S11 B and E) and mixing (Figures S11 C and F). The x-axis on all plots denotes the position along the colon along the first 50cm. It is clearly visible that growth occurs (i.e. bacterial densities increase in Figures S11 A-C) only in the first part of the colon, where nutrients are abundant. For very fast flow (Figure S11 A, black line), very slow bacterial growth (Figure S11 B, yellow line) and very weak mixing (Figure S11 C, pink line), high bacterial density cannot stably be maintained, and washout occurs. As it is not possible to reach high bacterial densities in those conditions, nutrients are not consumed, which is reflected by the rising nutrient levels (Figures S11, D-F).

Given the estimated flow velocity profile in the large intestine (see SI 2.2, Figure S10), we expect dynamics in the proximal colon to occur close to this washout condition. In the following, we therefore analyze the washout scenario in more detail, taking the predicted flow velocity profiles due to water absorption (see SI 2.2) into account. The main difference to the scenario shown in Figure S11 (no water absorption, constant flow velocity) is the concentrating effect that water absorption has on bacteria as well as nutrients; with water absorption, the same nutrient inflow (see SI 2.6) can lead to much higher local concentrations of nutrients as well as bacteria, with bacterial densities reaching much higher values, resembling densities reported in the literature (37, 38).

The simulation results are shown in Figure S12. Shown are nutrient abundance and bacterial density for varied velocity profiles, growth-rates, and mixing.

The present mixing dynamics has another important consequence for modeling. Taking the estimated effective diffusion ($D = 100 \cdot 10^4\,\mu m^2 s^{-1}$), the time scale required to reach the boundary of the ascending colon (distance $\Delta x = 0.5 \cdot d_{pLI} = 1.3\,cm$) is given by $11\,min$. This is a time scale faster than growth. Mixing does help to overcome distances from SCFA to the epithelial layers and thus ensures an efficient uptake of the latter. This mixing also justifies the approximation by a 1D model where we don't take the directions perpendicular to the main flow-flow into account explicitly.

To further illustrate the role of mixing and flow-profiles on growth dynamics, we analyzed growth dynamics when varying both, mixing and flow-profile. Since growth is happening mostly in the proximal large intestine, we focus on this regime in the following. For our analysis we consider the average flow velocity in the proximal large intestine, $\bar{v}_{prox}$. If follows as $\bar{v}_{prox} = l_{asc}/t_{T,asc}$ from the transit time through the proximal large intestine. The transit time in turn is a direct consequence of the velocity profile. For a linear velocity profile as introduced in SI 2.2 the transit time is given by:

$$t_T = \int_{x=0}^{x=l_{asc}} \frac{dx}{v(x)} = -\frac{1}{v'} \ln\left(1 - \frac{v' \cdot x_c}{v_{in}}\right) + \frac{l_{asc} - x_c}{v_{out}} \quad (2)$$

Here, $x_c = (v_{in} - v_{out})/v'$ denotes the point where the velocity profile becomes constant. Transit time and thus average flow velocity can be changed by variation of v_{in}, v_{out}, and v'. The average flow velocity along the proximal large intestine is shown in Figure S13. In the following we change the average flow velocity by changing the water absorption rate, v'. For changing mixing and absorption the average bacterial density in the proximal large intestine is shown in Figure S2.

2.6 Nutrients reaching the large intestine

Nutrients for bacterial growth in the large intestine are mostly supplied by nutrient inflow from the ileum. For a western diet it is estimated that 50-60g of carbohydrates reach the colon every day (39, 40). Two major forms of carbohydrates are distinguished, fibers and resistant starch. From the daily carbohydrate loads, about 20g per day are fibers (41, 42), of which about 75% are metabolized in the colon (43). The remaining carbohydrates (35-50 g/day) enter in the form of resistant starch and other sugars that failed to be taken up in the small intestine. For these carbohydrates, utilization is higher (39, 44).

Nutrient inflow can change considerably, depending on the diet. In particular, inflow of carbohydrates can be very different for non-western diets (41). Nutrient inflow can also change with a shift in eating behavior for a similar overall diet. Such shifts can include changes in calorie consumption (45), or changes in the composition of carbohydrates, for example the introduction of high fructose corn syrup (46) or the use of low calorie sweeteners (47).

As a reference condition we here assume a western diet with a supply of 55g carbohydrates into the colon. 55g carbohydrates and an inflow rate of $Q_{il} = 1.5\, l \cdot day^{-1}$ corresponds to an average inflow concentration of $n_{in} \approx 200\, mM$ glucose equivalents, or a total inflow of $300 mmol \cdot day^{-1}$ of glucose equivalents. For the range of calorie consumption among healthy humans and within single individuals over time, we assume a daily nutrient inflow varying between 100 and $600\, mmol$. With $300\, mmol/day$ of glucose equivalents being the colonic nutrient inflow of a standard western diet, the range we assume spans everything from one third to double the average inflow of our estimate of a standard diet.

2.7 Approximating growth conditions in the proximal large intestine

The bacterial phyla that we are considering here (Bacteroidetes and Firmicutes), and which account for roughly 90% of the microbial cells typically found in the human colon (48), are both able to digest a range of carbohydrates (26, 49, 50). As a first approximation of the growth dynamics, we thus do not take differences in the capacities of the different strains to digest fibers into account. On the coarse-grained level of our model, we consider nutrient concentrations in terms of glucose equivalents and use measured growth rates for growth on glucose. For some well-characterized strains like *Escherichia coli*,

growth rates depend strongly on the chosen carbohydrates. However, we note that growth rates of the two strains used in this study (*Er* and *Bt)* vary little when replacing glucose by starch. Starch is the major source of carbohydrates in most diets and large amounts of starch have been shown to reach the colon SI 2.6; in contrast, most mono and disaccharides are absorbed efficiently in the small intestine and do not play an important role for bacterial fermentation in the colon. We measured growth rates on starch at pH 7 to be $0.96\ h^{-1}$and $0.87\ h^{-1}$for *Bt* and *Er* respectively (as compared to $1.04\ h^{-1}$and $0.76\ h^{-1}$ for growth on glucose, Fig. 1). This relatively small change has also been confirmed for other abundant gut bacteria (51). Further, the observed strong pH dependence of growth rates (with growth rates going down to 10% of max growth rates for physiologically relevant pH ranges, see Fig. 1C) has also been observed for growth on starch (51). Combined these observations suggest that the pH effect on growth focused on in this study is important and dominants over changes in growth-rates via variation of the major carbohydrate composition in many situations.

To further mimic growth-conditions in the proximal large intestine, we used growth medium supplemented with amino acids (in the form of tryptone, see Materials and Methods). Using such a complex medium is realistic: First, the ileal effluent is known to contain amino acids and proteins which have not been absorbed by the small intestine (52, 53). Second, as indicated for example by the increase of branched chain fatty acids (products of amino acid fermentation (54)) in the distal colon (55), growth dynamics in the distal colon is slower and mostly based on digestion of amino acids, indicating that amino acids are not depleted in the proximal intestine. This is also supported by the fact that *Bt* and *Er* cannot use amino acids as sole sources of carbon and energy, even though *Er* cannot grow without amino acids in the medium (data not shown). Strong growth in the proximal intestine, the focus of our analysis, is mainly limited by the availability of carbohydrates. The medium used for our growth experiments and our modeling approach is based on this.

The additional growth conditions (constant temperature at 37°C, controlled osmolality of approximately $0.29\ Osm$ (56)) also emulate conditions in a healthy human colon.

2.8 pH regulation by the epithelium: SCFA uptake and bicarbonate excretion

SCFA Uptake rates of the epithelium have been measured in vivo and in vitro. Measurements in the human colon employing dialysis membranes have been performed to estimate the uptake rates of different short chain fatty acids (57). Measured rates are between $1.4\ldots 8.1\mu mol\cdot cm^2\cdot h$ for different SCFA under various conditions (Table 2 in (57)). In vitro studies confirm a total uptake rate of the same order, $9\frac{\mu mol}{cm^2\ h}$, with absorption rates not differing much for different SCFA (40).

There are different mechanisms for SCFA to enter the epithelial cells lining the colon (see (58) for a recent summary); one possibility is passive diffusion of SCFA through the epithelial membrane. However, for physiological pH ranges in the colon, more than 99% of SCFA are present in the deprotonated (i.e. charged) form. As only uncharged particles can effectively diffuse through cell membranes, passive transport is expected to play only a minor role and we do not include it into our model.

A second and likely more important way of SCFA uptake is transport through proteinaceous membrane channels. In particular, exchange of SCFA for bicarbonate and other ions via antiporters in the gut epithelium has been described, with most of the imported SCFA being exchanged for bicarbonate (57, 59). This is important for our model, since bicarbonate can counteract the acidification of the bacterial

growth environment by buffering the effect of the secreted SCFA on local pH, see SI 4. Km values for this type of transport have been measured to be of the order, $K_{m,SCFA} = 1.5\ mM$ (59).

In our model, we consider uptake of all SCFA by a combined uptake rate following a Michaelis-Menten kinetics with a spatially homogenous maximum uptake rate given by $20\ \mu mol \cdot cm^{-2} \cdot h^{-1}$. See SI 5.5 for our mathematical implementation.

In this context, we also note that to estimate the major turnover of SCFA in the gut, SCFA uptake by cross-feeding bacterial cells in the colon can be neglected to a first approximation. The reason is the impeded growth of cells cross-feeding on SCFA: The low energy amount of SCFA compared to the primary carbohydrates allows only for very slow growth which in the presence of strong flow does not allow accumulation of the cross-feeding cells to high densities (see SI 2.5 for discussion on the subject of "washout"). The low abundances of these cells result in low SCFA uptake compared to the other processes considered in this work.

E. rectale as representative of Firmicutes have been discussed to actively consume acetate (26, 60). However, when growing this strain in the presence of starch, glucose, and acetate we find that the net acetate-level increases at about the same rate (data not shown). While this does not exclude uptake of acetate, the results of this uptake on luminal SCFA concentration is not relevant for our analysis.

2.9 Back-diffusion of carbon dioxide into the epithelium

Permeabilities of carbon dioxide have been measured for the apical epithelial membranes of the proximal and distal colon in guinea pigs (61). The permeability is in the range $P_{CO2} \sim 10^{-3}\frac{cm}{s}$ and is higher in the proximal than in the distal colon. In the absence of active CO_2 flow, this permeability would lead to a luminal CO_2 concentration that slowly approaches levels measured in blood (approximately 1.35 mM (62)). However, this diffusion of CO_2 is happening on similar timescales as CO_2 production through bacterial growth (see SI 3.2) and bicarbonate release by active transport (see SI 2.8). This not only leads to a buffering of pH by bicarbonate for fast growth, but also to neutral pH values and falling luminal CO_2 for slow growth.

The time-scale for this process depends on the permeability and the diameter of the luminal tube, as is further analyzed in SI 5.6. As expected, Endeward and Gross observed a much lower permeability for bicarbonate than for gaseous CO_2 (61). For the simulations, we thus take only the permeability of gaseous CO_2 into account.

3 Modeling of bacterial growth

Experimental procedures of growth rate characterization are described in detail in the Methods section. Experimental results are shown in Figures 1 and S1. Growth conditions are discussed further in SI 2.6. In this section, we describe how we integrated these measurements into our model description.

3.1 Results of bacterial measurements

The central metabolic pathways for the strains used in this study are described (26, 63-65), and we show a simplified illustration of these pathways in Figure S1 AB. In Table S2, we summarize the most important measured physiological parameters for the two strains used in this study.

For growth rate depending on pH we fitted a logistic curve:

$$\lambda(pH) = \lambda_m \varphi(ph) = \frac{\lambda_{max}}{\left[1 - e^{-k_g(pH - pH_g)}\right]}. \quad (3)$$

The fit is shown in Figure 1. All excretion and yield values are mean values averaged over the different pH conditions measured. As shown in Figure S1, these values do not vary much with pH.

3.2 Carbon dioxide production

In order to model bacterial CO_2 excretion, we assume that the measured excretion rates of fermentation products reflect all the active fermentation pathways in the two strains, and calculate the corresponding net CO_2 production according to the pathways shown in Figures S1 A and B. In this picture, one molecule CO_2 is produced for every molecule acetate (1mM CO_2 per mM acetate). One CO_2 is consumed to produce succinate (-1mM CO_2/mM succinate), which can be reclaimed by converting succinate to propionate (0mM CO_2/mM propionate). Lactate production is CO_2 neutral (0mM CO_2/mM Lactate), whereas butyrate production from 2 acetyl-CoA leads to the production of 2 CO_2 (2mM CO_2/mM butyrate). Using these relations, we can calculate the CO_2 production through bacterial growth, ϵ_{CO2} based on the observed secretion profiles.

$$\epsilon_{CO2}^{B/F}(x,t) = \epsilon_{acet}^{B/F} + 2 \cdot \epsilon_{buty}^{B/F} - 1 \cdot \epsilon_{succ}^{B/F} \quad (4)$$

The values are shown in Table S2.

4 Buffer behavior of the lumen and pH

As pH can strongly affect bacterial growth (see SI 3.1 and Figure 1) it is important to explicitly model buffering behavior. Besides the SCFA excreted by bacteria during growth, buffer behavior of the lumen through bicarbonate is the most important factor setting the local pH in the lumen. The possible role of buffer to optimize bacterial growth, including the role of bicarbonate, has been suggested before (44, 58, 66). For the earlier studies, the role of the epithelial transporters was still not known, but accumulation of carbonate was observed during transportation of SCFA. More recent work has confirmed this picture (see SI 2.8 about SCFA uptake). Here, we analyze the buffer behavior of the lumen and the role of bicarbonate for varying SCFA concentrations. The following description for buffer dynamics is used in the final model to calculate local luminal pH.

Carbon dioxide, carbonic acids and bicarbonate are important parts of the blood buffering system (67, 68). In a similar way, this carbon dioxide/bicarbonate/carbonic acid buffering system is likely to contribute to the buffer behavior in the lumen. In a simplified approach, we here consider only the effective reaction between carbon dioxide and bicarbonate,

$$HCO_3^- + H^+ \rightleftharpoons H_2O + CO_2 \quad (5)$$

with an effective $pK_a = 6.2$. In the following, we denote the concentration of this buffering system, including carbon dioxide, carbonic acid and bicarbonate, as total carbonate. Importantly, carbonate is not working as buffer system alone, but also other luminal contents play important roles (69-71). Again this is similar to buffer dynamics in the blood where other components (especially proteins in the plasma and erythrocytes) are thought to contribute strongly to buffer capacity (62). For the lumen, it is unclear which components contribute to this additional buffer capacity and a shift to neutral pH levels. Thus, we here include buffer behavior of lumen using a phenomenological description, which does not

take single components of the lumen into account but considers luminal contribution to buffer behavior by a measured buffer capacity. The buffer behavior is described by a function relating pH to added protons. In the simplest case, the relation is linear, that is the pH changes with added free protons, H_A^+, according to

$$pH = W[s, c] \equiv pH_0 - \beta_{buffer}^{-1} H_A^+[s, c, pH] \quad (6)$$

with pH_0 being the pH when no additional protons are supplied (by SCFA or carbonate). The buffer capacity β_{buffer} can be measured by observing change in pH when adding a strong acid. Such measurements have been done for luminal fluids in different parts of the intestine (69-71). Buffer capacity in the ileum is given by approximately $\beta_{buffer,il} = 5 - 10\ mM \cdot pH^{-1}$ (69). Higher values have been measured for the ascending colon, $\beta_{buffer,cln} \approx 30\ mM \cdot pH^{-1}$ (69). This change can be explained by changing buffer concentrations alone: water absorption in the proximal colon leads to a higher concentration of buffer components in the ascending and transverse large intestine, when comparing it to concentrations in the ileum or cecum. Given an inflow of $Q_{il} \approx 1.5l \cdot day^{-1}$ and fecal outflow of $Q_{fec} \approx 0.1l \cdot day^{-1}$ (see SI 2.2), this means that buffer concentrations can increase by a factor 15 provided no buffer components are lost (e.g. by uptake into the epithelium). In the simulations we approximate the buffer capacity by a constant value and work with a buffer capacity expected at the end of the ascending colon (the main growth zone), $\beta_{buffer} \approx 100\ mM \cdot pH^{-1}$. Measurements also confirm a neutral pH for the low SCFA and bicarbonate levels in the ileum, $pH_0 = 7.4$ (72).

Both, SCFA and total carbonate contribute to the free proton pool, which has to be buffered by the luminal basal buffer capacity. The dissociated protons, which have to be buffered, depend on the pH values and the pK_a values of SCFA and total carbonate (described by the Henderson-Hasselbalch equation). Thus, for the physiological range in the colon (pH 5.5-7.4), most of the SCFA ($pK_a \approx 4.8$) are present in ionized form. In contrast, for carbonate, this can be shifted because of the larger $pK_a \approx 6.2$. For pH values below the pK_a of the carbonate system, less and less of the carbonate is present in dissociated form, and thus contributes less to the free proton pool. If adding additional carbonic acid, not all ends up contributing to a decrease in pH. Hence, the bicarbonate acts as a buffer against lower pH values.

For a given total concentration of carbonate (C_C) and SCFA (C_S), and pK_S and pK_C being the pK_a values for SCFA and carbonate, respectively, the total amount of additional protons, which need to be compensated by the luminal buffer, is thus given by:

$$H_A^+ = C_S \frac{10^{pH-pK_S}}{1 + 10^{pH-pK_S}} + C_C \frac{10^{pH-pK_C}}{1 + 10^{pH-pK_C}} \quad (7)$$

The final pH is given by a self-consistent solution of both equations. This is achieved numerically by iteration. For the buffer-capacity observed in the human gut, the resulting relation between SCFA, total carbonate and pH is shown in Figure S14.

5 Mathematical model and implementation

We here introduce details of the underlying mathematical model to simulate growth and uptake dynamics in the colon. A short summary of the model structure is also given in the Methods section.

We model the dynamics by an effectively one-dimensional model. x denotes the position between the ileocecal valve/cecum ($x = 0\ m$) and the rectum ($x = l_{LI}$). t denotes time. We include the following variables into our model:

i. Bacterial densities of strains $\phi = \{B, F\}$, $\{\rho^{\phi}(x,t)\}$. Here, we distinguish between densities of *Firmicutes (Er)* and *Bacteroidetes (Bt)*, $\rho^{F}(x,t)$ and $\rho^{B}(x,t)$.
ii. Nutrient density, $n(x,t)$.
iii. Total short chain fatty acids concentration, $s(x,t)$.
iv. Total carbonate, the sum of dissolved carbon dioxide, carbonic acid and bicarbonate. Denoted by $c(x,t)$.

pH is not modeled explicitly but follows given the current abundance of short chain fatty acids and total total carbonate, see SI 4.

5.1 Modeling flow and peristaltic mixing

We consider the spatiotemporal evolution of all variables, $\{\rho^{\phi},\ n, s, c\}$. Mixing and flow is described by convection and diffusion terms. For example, bacterial density of strain $\phi = \{B, F\}$ follows the equation

$$\partial_t \rho^{\phi} = D\partial_x^2 \rho^{\phi} - \partial_x v\ \rho^{\phi} + f_{\rho}^{\phi}(\rho, n) \tag{8}$$

Flow is considered by a convection term proportional to the flow velocity, v. Related to water-absorption, flow decreases distally and flow velocity is a function of position, $v = v(x)$, see SI 2.2. Mixing is modeled by a term proportional to an effective diffusion coefficient, D. This simplified phenomenological description of complex mixing dynamics by wall-contractions with an effective diffusion approach has been successfully applied in an in-vitro setup to study intestinal mixing and growth (5). Importantly, the effective diffusion coefficient depends on the underlying dynamics of the flow and is not only a function of microscopic parameters. We estimate it by observation of flow and mixing dynamics in the proximal colon, see SI 2.4. $f_{\rho}^{\phi}(\rho, n, pH)$ denotes the source term. Source terms for all variables, $\left\{f_{\rho}^{\phi}, f_n, f_s, f_c\right\}$, are introduced in the following sections.

5.2 Boundary conditions

Boundary conditions are chosen to match the known inflow and outflow conditions of bacteria and nutrients in the large intestine. At the inlet $(x = 0)$ there is zero bacterial and SCFA influx, $j_{\rho}^{\phi}(x = 0) \equiv -D\partial_x \rho^{\phi}\big|_{x=0} + v\rho^{\phi}(x = 0) = 0$, and $j_s(x = 0) \equiv -D\partial_x s|_{x=0} + vs(x = 0) = 0$. Nutrient flux is fixed, $j_n(x = 0) \equiv -D\partial_x n|_{x=0} + v\ n(x = 0) = v\ n_{in}$. See SI 2.6 for considerations of nutrient inflow concentration, n_{in}. At the outlet, $(x = l_{LI})$, there is an unobstructed outflow of bacteria, nutrients and SCFA; diffusive flux is zero: $j_{\rho}^{\phi}(x = l_{LI}) \equiv -D\partial_x \rho^{\phi}\big|_{x=l_{LI}} = 0$, $j_n(x = l_{LI}) \equiv -D\partial_x n|_{x=l_{LI}} = 0$, and $j_s(x = l_{LI}) \equiv -D\partial_x s|_{x=l_{LI}} = 0$.

5.3 Bacterial growth and nutrient depletion

The dynamics is modeled to follow Monod type kinetics (4):

$$f_{\rho}^{\phi}(\rho, n, pH) = \lambda^{\phi}(n, pH)\rho^{\phi} = \lambda_{max}^{\phi}\varphi^{\phi}(pH)\frac{n}{n + K_m^{\phi}}\rho^{\phi} \tag{9}$$

$$f_n(\rho, n, pH) = \sum_{\phi=\{B,F\}} \frac{\lambda^\phi(n, pH)}{Y^\phi}\rho^\phi = \sum_{\phi=\{B,F\}} \frac{\lambda^\phi_{max}}{Y^\phi}\varphi^\phi(pH)\frac{n}{n + K_m^\phi}\rho^\phi \qquad (10)$$

In these equations, λ^ϕ_{max} denotes the maximal growth rate of strain $\phi = \{B, F\}$, Y^ϕ denotes the yield of strain ϕ, and K_m^ϕ is the Monod constant of strain ϕ. We model the pH dependence of growth, $\varphi^\phi(pH)$, to follow a logistic fit, see SI 3.1 and Figure 1. The parameters are derived from the growth experiments with *Er* and *Bt*, listed in Table S2.

5.4 The mucus layer as a limiting factor of SCFA uptake

As described in SI 2.4, mixing is continuously occurring in the proximal colon and leads to well mixed behavior on local scales. In particular, strong gradients perpendicular to the flow-directions cannot build up due to mixing. This is however only the case in the lumen. Mixing is limited close to the epithelial cells: the mucus layer at the colon walls defines a region where diffusion might limit uptake of acetate and other SCFAs. To consider this effect, we include a diffusive region with a thickness d_{muc} between epithelial cells and lumen.

Thickness of the mucus layer can be approximated using ex vivo measurements, $d_{muc} \approx 400\mu m$ (73, 74). Diffusion within the mucus layer is reduced compared to normal diffusion. In vitro measurements of diffusion of butyrate in rat mucus estimate $D_{muc} = 3 \cdot 10^{-10} m^2 s^{-1}$. This is about 25% of the diffusion constant in water. Theoretical studies have also estimated the diffusion rate in mucus and came to a similar conclusion, see e.g. (75).

We mathematically include this diffusion process as described in the following paragraph. Here we discuss the solution, shown in Figure S15. For large concentrations of SCFA in the lumen, uptake rate is limited by the uptake rate of epithelial cells. This changes for lower SCFA concentrations. Below a certain value, which depends on the thickness of the mucus layer, uptake becomes limited by the mucus layer. For a mucus thickness of $d_{muc} = 400\mu m$, this concentration is given by about 30mM. As an example, the figure shows the behavior for acetate. In the human large intestine, acetate concentrations vary between approximately 20 and $200mM$. Thus, the relevant SCFA concentration is in the range where the mucus layer can limit fast uptake. However, in the proximal colon, where growth is strong and SCFA levels are high, the diffusion barrier is of minor importance.

In the remaining paragraphs of this section, we describe how we mathematically consider the mucus layer as a diffusion barrier for SCFA uptake (the derived results are shown in Figure S15).

With s_{muc} denoting SCFA concentrations in the mucus layer, and z denoting the distance from the epithelial cells, the diffusion dynamics in the mucus layer is given by:

$$\partial_t s_{muc}(z) = D_{muc}\partial_z^2\, s_{muc}(z) \qquad (11)$$

The boundary conditions are given by $s_{muc}(z = d_{muc}) = s_{lum}$ and $j_{SCFA} \equiv -D_{muc}\partial_z s_{muc}(z)|_{z=0} = -j_{SCFA,max}\frac{s_{muc}(z=0)}{s_{muc}(z=0)+K_m}$. Here, $j_{SCFA,max}$ denotes the maximal uptake flux by the epithelial cells if SCFA concentrations and diffusion flux are not limiting uptake (in the remainder of this section we denote it simply by s_{max}). s_{lum} denotes the concentration in the well-mixed lumen (in other sections this concentration is denoted simply by s). The full steady state solution is given by a linear profile, $s_{muc}(z) = s_{muc}(z = 0) + \varkappa z$. From boundary condition $s_{muc}(z = d_{muc}) = s_{lum}$ it follows $\varkappa =$

$\frac{j_{max}}{D}\frac{s_{muc}(z=0)}{s_{muc}(z=0)+K_m}$. With that and the second boundary it follows the quadratic equation: $s_{muc}(z=0)^2 + s_{muc}(z=0)\cdot\left(K_m - s_{lum} + \frac{j_{max}\,d_{muc}}{D}\right) - s_{lum}K_m = 0$. The solution is given by $s_{muc}(z=0) = \frac{1}{2}\left(s_{lum} - \tilde{j} - K_m + \sqrt{4s_{lum}K_m + (-s_{lum} + \tilde{j} + K_m)^2}\right)$ with $\tilde{j} = \frac{j_{max}d_{muc}}{D_{muc}}$. Note that consistently, $s_{muc}(z=0) = s_{lum}$ for a vanishing mucus layer, $d_{muc} = 0$. Given the local concentration at the epithelial layer, $s_{muc}(z=0)$, one can then calculate the uptake rate

$$j_{SCFA}(s) = j_{max}\frac{s_{muc}(z=0)}{s_{muc}(z=0)+K_m}. \tag{12}$$

This relation is shown in Figure S15. In our simulations, we included this relation, see also the following SI 5.5.

5.5 Short chain fatty acid dynamics

The production and uptake of short chain fatty acids is given by

$$f_s(\rho,n,s,pH) = \sum\nolimits_{\phi=\{B,F\}} \lambda^{\phi}_{max}\epsilon^{\phi}_{SCFA}\varphi^{\phi}(pH)\frac{n}{n+K^{\phi}_m}\rho^{\phi} - J_{SCFA}(s) \tag{13}$$

The first term considers the production of short chain fatty acids by bacterial growth. The second term models the uptake of SCFA by the epithelial cells. By accounting for a constant ratio between the volume of the channel (where SCFA are produced) and its surface (where the uptake takes place), which is $d_{lum}/4$, where d_{lum} is the diameter of the luminal tube, we introduce an effectively 3-dimensional uptake rate, $J_{SCFA}(s) = \frac{4}{d_{lum}}$. $j_{SCFA}(s)$ is the effective SCFA uptake rate considering the diffusion boundary by the mucus layer, see previous section SI 5.4 See Table S2, SI 3.1 and SI 2.8 for parameter estimations.

5.6 Carbon dioxide balance

Total bicarbonate concentration (bicarbonate, carbonic acid and CO_2) follows the same convection and diffusion dynamics as bacteria, nutrients and SCFA. The source term is given by the following:

$$\begin{aligned} f_c(\rho,n,s,c,pH) &= \sum\nolimits_{\phi=\{B,F\}} \lambda^{\phi}_{max}\epsilon^{\phi}_{CO2}\varphi^{\phi}(pH)\frac{n}{n+K^{\phi}_m}\rho^{\phi} + u(s,c,pH) \\ &\equiv \sum\nolimits_{\phi=\{B,F\}} \lambda^{\phi}_{max}\epsilon^{\phi}_{CO2}\varphi^{\phi}(pH)\frac{n}{n+K^{\phi}_m}\rho^{\phi} + \alpha_c\cdot J_{SCFA}(s) + e_c(c,pH) \end{aligned} \tag{14}$$

Here, the first term denotes the carbon dioxide produced by bacteria during growth; see SI 3.2 for an estimation of the excretion rates, ϵ^{ϕ}_{CO2}. The second term considers release of bicarbonate from the epithelial cells, coupled with the uptake of SCFA. Here, α_c denotes the fraction of SCFA transporters that are anti-porters, releasing bicarbonate in the same amount as SCFA ions are taken up. The third term describes back diffusion of carbon dioxide through the epithelial layer: besides the modeled outflow of total bicarbonate, carbon dioxide can leave the lumen via the gas phase, or by diffusion through the epithelium. In the following we drive this excretion function, $e_c(c)$:

Given a section of the laminar tube with length dl, volume V_{dl} and surface area A_{dl}, the net movement of CO_2 through the epithelial membrane is given by: $\partial_t c_{dl} = -P_{CO2}\cdot A_{dl}\left(c_{dl} - c_{ep}\right)\cdot V_{dl}^{-1}$. Here, c_{dl}

and c_{ep}describe CO_2 concentrations in the pipe section and the underlying epithelial layer. The CO_2 in the lumen follows from the total bicarbonate concentration (bicarbonate and dissolved CO_2) and depends on pH (see also SI 4 where buffer dynamics is explained). In addition, surface area and volume of the tube section depend on the diameter of the lumen, d_l.

$$e_c(c, pH) = -\frac{4}{d} P_{CO2} \cdot \left(\frac{1}{1 + 10^{pH - pK_a}} c - c_{ep} \right) \tag{15}$$

The rate of back diffusion is given by $\kappa_{CO2} \equiv \frac{4}{d} P_{CO2}$. For a permeability in the range of $P_{CO2} = 10^{-3}..10^{-5}\ cm \cdot s^{-1}$, the rate lies in the range $2 \cdot 10^{-3} - 10^{-5} \cdot s^{-1}$. This rate is of the same order as bacterial growth, $\lambda \sim \frac{1}{h}$.

5.7 Estimation of different SCFA concentrations and uptake

We approximate the local concentrations of specific SCFA by the total SCFA concentration, $s(x,t)$, the local abundance of both strains, $\rho^{B/F}$, and the measured excretion rates of both strains. We denote the local fractional of strains by $\alpha_B = \rho^B/(\rho^B + \rho^F)$ and $\alpha_F = (1 - \alpha_B)$. With that the local abundance of acetate is for example given by

$$s_{acet}(x,t) \approx \frac{\alpha_B\, \epsilon^B_{acet} + \alpha_F\, \epsilon^F_{acet}}{\alpha_B\, \epsilon^B_{SCFA} + \alpha_F\, \epsilon^F_{SCFA}} s(x,t) \tag{16}$$

Similar expressions hold for the abundance of other short change fatty acids. Uptake rate of SCFA depends on the local concentration (see SI 5.5). With this, the total uptake rate along the whole colon is given by

$$\dot{S}(t) \approx \pi \cdot d_{lum} \cdot \int j_{scfa}\big(s(x,t)\big) dx \tag{17}$$

Uptake rates of different SCFA are estimated by the local fractions of different SCFA. For example for acetate, uptake is given by $\dot{S}_{acet}(t) = \pi \cdot d_{lum} \cdot \int \frac{s_{acet}(x,t)}{s(x,t)} \cdot j_{scfa}\big(s(x,t)\big)\, dx$.

Energy uptake can be estimated by combustion enthalpy measurements for different fermentation products. For example, the energy uptake by acetate is given by $\dot{E}_{acet}(t) = H_{acet} \cdot \dot{S}_{acet}(t)$. The combustion enthalpies, $H_{\{SCFA\}}$, are listed in Table D. Comparisons are done between energy uptake and energy of nutrient inflow. The latter is given by $\dot{E}_{n_{in}}(t) = H_{gluc} \cdot \dot{N}_{acet}(t)$ and the combustion enthalpy of glucose, $H_{gluc} = 0.67\ kcal/mmol$.

Table D Property of main fermentation products. Data from(76). Throughout the text, we use total short chain fatty acids to include all fermentation products listed here.

Short chain fatty acid	Short notation $\{SCFA\}$	Combustion energy $H_{\{SCFA\}}$ (kcal/mmol)	$pK_{a,\{SCFA\}}$	Molar mass (g/mol)
Acetate	$acet$	0.21	4.76	60.05
Butyrate	$buty$	0.52	4.82	88.11
Lactate	$lact$	0.33	3.86	90.08
Propionate	$prop$	0.37	4.88	74.08
Succinate	$succ$	0.36	4.2	118

5.8 Relation of transit time with Bristol Stool Scale

The Bristol Stool Scale (BSS) has been introduced as a simple scale to classify human feces (77). It ranges from 1 to 6 with increasing water content (1 is very solid, 6 is very watery). The BSS varies strongly between individuals and within individuals over time. Typical ranges are between 1 and 5 for healthy humans with the most common values between 3-4 (78).

The BSS has been shown to be a good proxy for colonic transit times, with transit times decreasing strongly with increasing BSS (77-79), i.e., more watery stools have shorter transit times. This observation is in agreement with what is expected from simple flow considerations: Higher water throughput in the large intestine is related to a larger flow velocity which directly translates to a shorter transit time. To quantify the relation between BSS and transit time, we here follow the observations by O'Donnell et al (79), and use data reported there to approximate the relation between transit time, t_T, and BSS by the linear relation $BSS = 6.52 - 0.0526\ \frac{1}{h} \cdot t_T$ plotted in Figure S5 A.

Transit time is a direct consequence of flow dynamics and velocity profiles in the colon. Thus, with a change in velocity profile (by differences in water-inflow, water-uptake, and water-outflow) BSS is changing as well. For a linear velocity profile as introduced in SI 2.2, the transit time is given by:

$$t_T = \int_{x=0}^{x=l_C} \frac{dx}{v(x)} = -\frac{1}{v'} \ln\left(1 - \frac{v' x_c}{v_{in}}\right) + \frac{l_c - x_c}{v_{out}} \tag{18}$$

Here, $x_c = (v_{in} - v_{out})/v'$ denotes the point where the velocity profile becomes constant. The relation is shown in Figure S5 BC for varying water uptake-rate v' and outflow velocity v_{out}. It can be seen that x_c, and thereby stool consistency, can be changed by varying any of the three parameters, v_{in} (indicating changing inflow volumes due to changes in water uptake in the small intestine), v_{out} (a combination of inflow into and water uptake in the colon) , or v' (a change in water uptake in the colon). As any of these physiological parameters (or a combination of the three) can affect BSS under a given condition, we have analyzed changes in all three parameters separately. Figure 5 in the main text shows the effect of changing colonic water uptake (i.e. changes in v') on microbiota composition, Figure S8 shows the effect of v_{out} and v_{in}.

5.9 Numerical solution

Numerical solution of the partial differential equations was done employing an implicit scheme using python and the module FiPy (80). Integration over time was performed with time steps $dt = 0.125\ s$ and a grid resolution with spacing $dx = 1\ mm$. The source code is attached as supplementary file named 'source_code.txt'.

Supplementary Tables

Table S1. Physiology of the human large intestine. Summary of parameters used for simulations. See supplementary text for a detailed discussion and references.

Sizes	Symbol	Value	Section SI
Length colon, average	l_{LI}	$189.5\ cm$	2.1
Length proximal colon	l_{pLI}	$29.8\ cm$	2.1
Diameter	d_{col}	1.94 cm	2.1
Diameter cecum and ascending colon	d_{asc}	$2.6\ cm$	2.1
Diameter transverse and distal colon	d_{dist}	$1.8\ cm$	2.1
Flow and Mixing Behavior	Symbol	Value	
Nutrient inflow concentration (in glucose units)	n_{in}	200mM	2.6
Flow velocity beginning ascending colon	v_{in}	$32\mu m/s$	2.2
Velocity gradient (by water absorption)	v'	$0.75\ \mu m\ s^{-1} \cdot cm^{-1}$	2.2
Velocity outflow	v_{out}	$5.26\ \mu m \cdot s^{-1}$	2.2
Effective diffusion (mixing by wall contractions)	D	$10^6\ \mu m^2\ s^{-1}$	2.4
Buffer behavior			
Buffer capacity	β_{buffer}	$100\ mM \cdot pH^{-1}$	4
Buffer basal pH	pH_0	7.4	4
pK SCFA	pK_{SCFA}	4.8	5.7
Carbon dioxide in epithelial layer	$[CO_2]_{ep}$	$2.3\ mM$	2.9
Permeability carbon dioxide	P_{CO_2}	$9\ \cdot 10^{-3} cm \cdot s^{-1}$	2.9
Uptake/Excretion			
Uptake rate SCFA	$j_{max,SCFA}$	$2.5\ 10^{-5}\ \frac{mol}{m^2 s}$	2.8

Km SCFA uptake	K_{SCFA}	$20\mu M$	2.8
Fraction bicarbonate SCFA	α_{SCFA}	80%	2.8
Mucus			
Thickness mucus layer	d_{muc}	$400\ \mu m$	5.4
Diffusion constant SCFA in mucus	$D_{muc,SCFA}$		5.4
Numerical parameter			
Total simulation time	t_{sim}	120 h	
Lattice points along whole colon	nx	1890	
Integration time step	dt	$0.125\ s$	

Table S2. Parameters describing bacterial growth physiology. All parameters except of Monod constants are based on direct measurements of *Bacteroides thetaiotaomicron* (*Bt*) and *Eubacterium rectale* (*Er*) strains. See Methods section for details of measurements and parameter deviations. Measurement results are shown in Fig. 1 and S1.

	Symbol	*B. thetaiotaomicron* ($\phi = B$)	*E. rectale* ($\phi = F$)
Max. growth rate	λ_{max}^{ϕ}	$1.051\ \mathrm{h}^{-1}$	$0.721\ \mathrm{h}^{-1}$
pH dependence growth, logistic fit, pH at max. change	pH_g^{ϕ}	5.83	5.50
pH dependence growth, logistic fit, max. change	k_g^{ϕ}	6.60	5.23
Acetate excretion	$\epsilon_{acet.}^{\phi}$	$4.805 \pm 0.317\ mM/OD$	$2.722 \pm 0.669\mathrm{mM/OD}$
Butyrate excretion	$\epsilon_{buty.}^{\phi}$	No measurable excretion	$4.727 \pm 0.493\mathrm{mM/OD}$
Lactate excretion	$\epsilon_{lact.}^{\phi}$	No measurable excretion	$3.914 \pm 1.037\mathrm{mM/OD}$
Propionate excretion	$\epsilon_{prop.}^{\phi}$	$1.125 \pm 0.298\ \mathrm{mM/OD}$	No measurable excretion
Succinate excretion	$\epsilon_{succ.}^{\phi}$	$3.176 \pm 0.537\ \mathrm{mM/OD}$	No measurable excretion
Total SCFA excretion	ϵ_{SCFA}^{ϕ}	$9.052 \pm 0.934\ \mathrm{mM/OD}$	$11.363 \pm 1.037\mathrm{mM/OD}$
Glucose consumption		$6.772 \pm 1.952\ \mathrm{mM/OD}$	$10.648 \pm 1.065\ \mathrm{mM/OD}$
Growth yield on glucose	Y^{ϕ}	$0.148 \pm 0.046\ \mathrm{OD/mM}$	$0.094 \pm 0.009\ \mathrm{OD/mM}$
Monod constant	K_m^{ϕ}	$50\mu M$	$50\mu M$
Carbon dioxide excretion	Y_{CO2}^{ϕ}	mM/OD	mM/OD

Table S3. Comparison of observed values and simulation results. Calculated values from simulations for reference scenario with same parameters as results shown in Figure 3, see Table 2 and 3. Ranges shown in parenthesis for variation of nutrient inflow-concentration and water-absorption rate as shown in Figures 4 and 5.

Observable	Observed range	Range in simulations	Reference
Bacterial density in cecum	$10^6 - 10^9 cells/g$	$10^8 - 10^9\ cells/g$	(25)
Bacterial density in feces	$3.2 - \ 5 \cdot 10^{11} cells/g$	$\sim 10^{11} cells/g$	(37, 38)
pH in the proximal colon	$4.9 - 5.9$	5.7 $(5.6 - 6.3)_{Fig.\ 3}$ $(5.2 - 6.7)_{Fig.\ 4}$	(55, 81)
pH in the distal colon	$5.8 - 6.7$	6.9 $(6.0 - 7.1)_{Fig.\ 3}$ $(6.8 - 7.0)_{Fig.\ 4}$	(55, 81)
Fecal pH	$7.3 - 7.5$	7.2	(82)
Max. SCFA concentration	$137 - 197\ mmol/kg$	$370\ mM$ $(120..540)_{Fig.\ 3}$ $(180..430)_{Fig.\ 4}$	(55, 81)

Table S4. Summary of parameter variations. To understand the importance of different physiological parameters in setting bacterial growth dynamics and microbiota composition and to understand which of these parameters most crucially affect microbiota composition we performed a sensitivity analysis by varying the different physiological parameters. In the following we list the parameter variations which are explicitly shown in this manuscript.

Variation	Reference
Variation of nutrient intake	See Figure 4
Variation of colonic water absorption	See Figure 5
Water entering and distally leaving the colon (inflow and outflow rate)	See Figure S8
Variation of mixing dynamics by different (changes in gut-motility).	See Figure S4
Variation of the luminal buffer capacity	See Figure S4
Variation of SCFA uptake	See Figure S4

Supplementary Figures

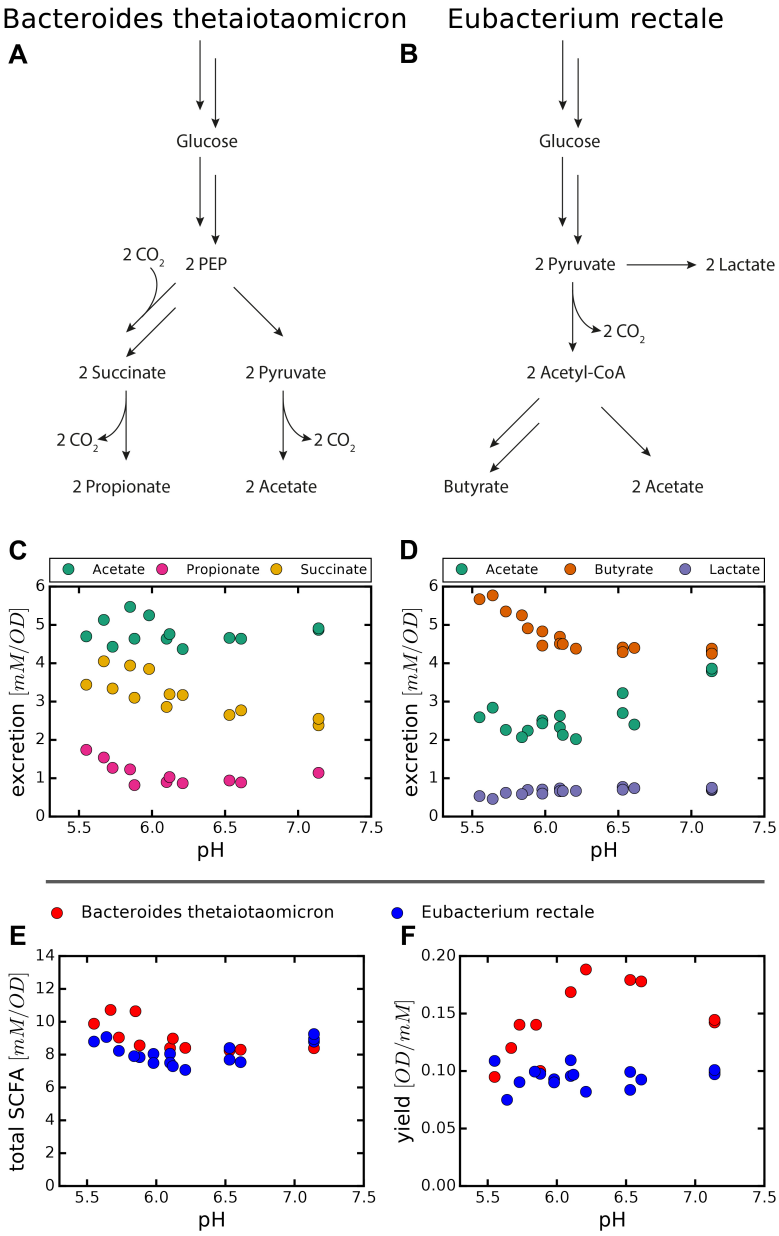

Figure S1. Growth dynamics of *Bacteroides thetaiotaomicron (Bt)* and *Eubacterium rectale (Er)*. (A) Pathways of fermentation in *Bt*, which can lead to acetate, propionate, and succinate as secreted end products. (B) Fermentation pathways in *Er*, with acetate, butyrate, and lactate as secreted products. CO_2 production and consumption is indicated for the different reactions. Adapted from (64). (C, D) Excretion rates of different fermentation products for *Bt* and *Er* respectively. (C) Sum of measured excretion rates. (D) Yield numbers. Cell density was measured by optical density at 600nm, ($1\ OD600 \approx 10^9\ cells/ml$). See methods section for experimental details.

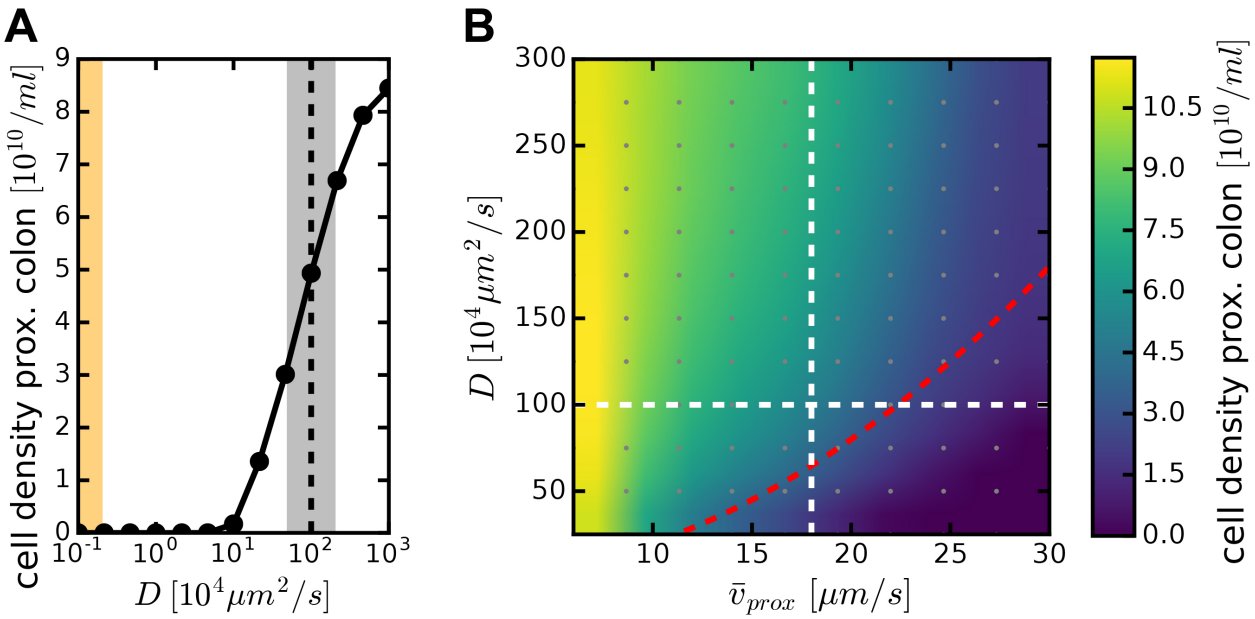

Figure S2. Effect of mixing on bacterial growth dynamics in the proximal colon

To illustrate the effect of mixing on bacterial growth dynamics we modeled growth of one strain in the colon under the influence of mixing and in the presence of a flow gradient. Active mixing by wall contractions is modeled by an effective diffusion D (see SI 2.4). (A) Average bacterial densities in the proximal colon depending on D. For values comparable to molecular diffusion ($D < 0.1\ 10^4 \mu m^2/s$, orange region) a dense population of bacterial cells cannot emerge because cells are washed out due to the strong flow. In contrast, for stronger mixing ($D \gtrsim 10 \cdot 10^4 \mu m^2/s$) a stable population can emerge in the proximal colon. We estimate the range of mixing in the human colon to $D = 50 - 200\ \mu m^2/s$ with $D = 100 \mu m^2/s$ used as standard value in simulations (shown as gray area and dashed line). This estimate is based on the analysis of published data (23), see Fig. S6 and SI 2.4. (B) Change in average bacterial density in the proximal colon for changes in both, mixing and flow dynamics. $\bar{v}_{prox}$ denotes the average flow velocity in the proximal colon. Standard parameters for healthy individuals as used in the model are shown as dashed white lines. The red line denotes the washout condition $\alpha = \frac{v^2}{D\lambda} \approx 1$, see SI 2.5 where the role of mixing- and flow-dynamics for bacterial growth is discussed in more detail. For illustration, the simulations here show simplified dynamics for only one strain and not including the pH feedback on growth dynamics via the accumulation of fermentation products; instead pH is assumed to be neutral, $pH = 7.2$, and growth is only limited by nutrient availability. Flow in (A) follows a profile as shown in Figure 2 and Figure S9. In (B) flow profile is changed by changes of the velocity gradient. $Y = 0.1\ OD/mM$, $\lambda_0 = 1\ h^{-1}$. Other parameters as in Table S1.

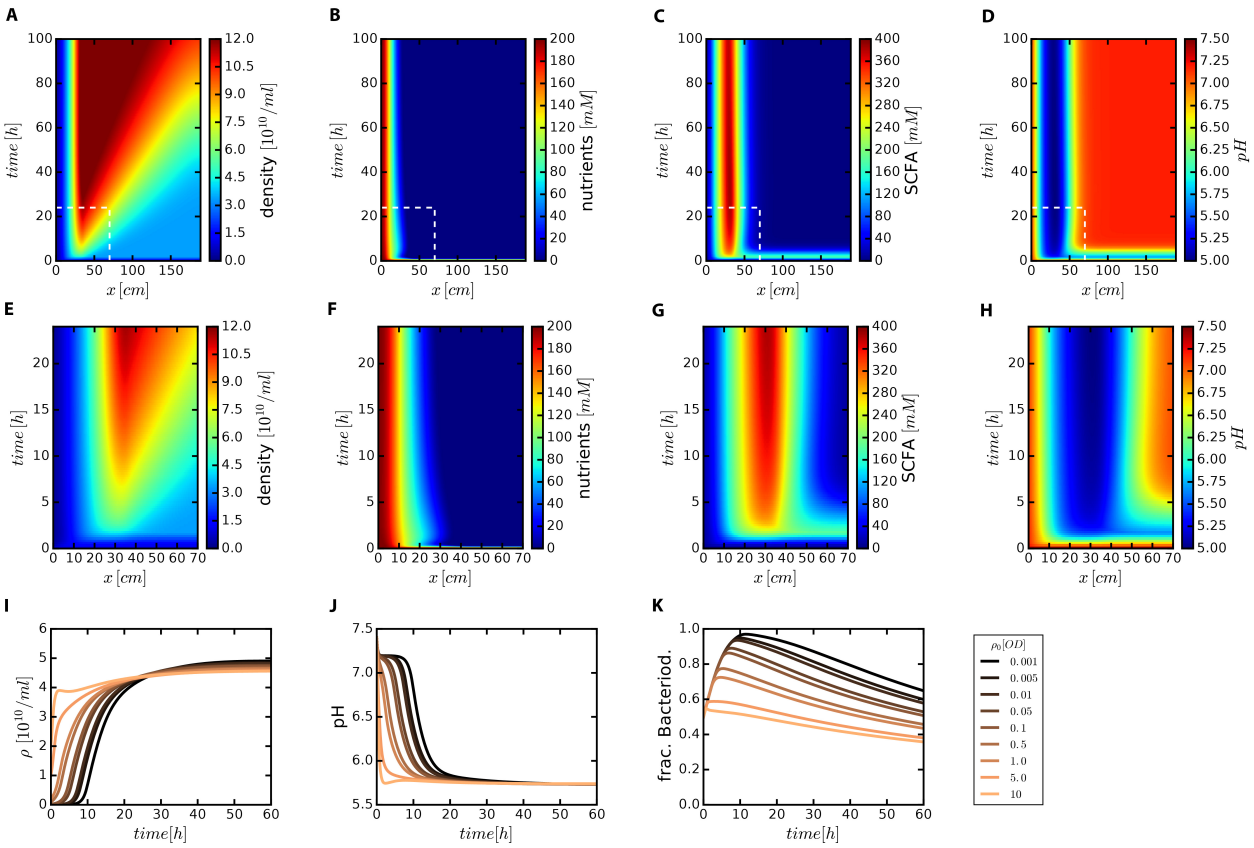

Figure S3. Changes in microbiota composition over time. (A)-(D) Kymographs showing full time evolution over the first 100 hours and the whole length of the colon. Initial density is $5 \cdot 10^9\ cells/ml$ with half of the cells being Fermicutes, half Bacteroidetes. In (E)-(H) the same data is shown, focusing on earlier times and the proximal colon. (I)-(K) Establishment of a stable microbiota population, starting with different low bacterial densities (color legend). Independent of initial density, a high bacterial density is reached within the first 24 hours. However, initial densities are affecting local pH values and thus also affect the abundance of the different phyla. For low initial densities, Bacteroidetes dominates initially. A stable coexistence with Firmicutes is only reached after several days. Parameters used are same as for Fig. 2 and are given in supplementary Tables S1 and S2.

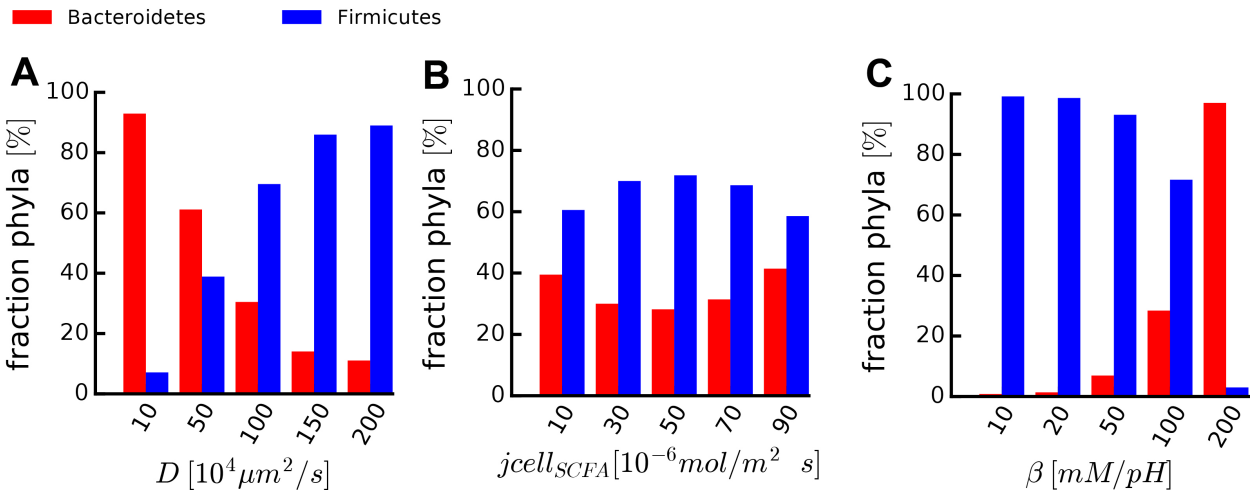

Figure S4. Changes in microbiota composition for variations in different physiological parameters. To understand the role of different physiological parameters we investigated the dynamics when changing key physiological parameters. (A) Change of strength of mixing in the colon (D). (B) Changes in uptake rate of short chain fatty acids through the epithelium ($j_{cell,SCFA}$). (C) Changes in buffer capacity of the luminal content (β). See SI 3 where further parameter variations shown in this study are listed. Standard conditions for mixing, SCFA uptake and buffer capacity are given by $D = 100 \frac{\mu m^2}{s}$, $j_{cell,SCFA} = 25 \cdot \frac{10^{-6} mol}{m^2\ s}$ and $\beta = 100\ mM/pH$; see Table S1.

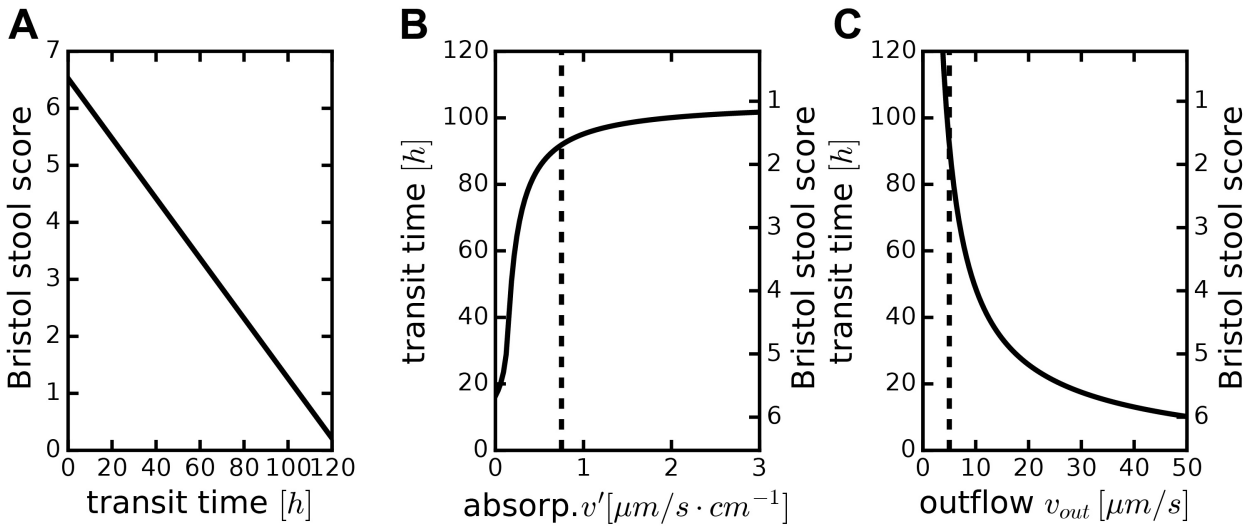

Figure S5. Relation between transit time and Bristol stool scale (BSS), and how those change with changes in flow-velocity profiles. (A) Observed relation between BSS and colonic transit time. This figure is based on data from (79) (B) Change of transit time and BSS when changing water absorption rate. (C) Change of transit time and BSS when changing outflow velocity. Used velocity profiles in (B) and (C) follow linear approximation with constant $v_{out} = 5\ \mu m/s$ in (B) and $v' = 0.75\,\frac{\mu m}{s} \cdot cm^{-1}$ in (C). See SI 5.8 for details.

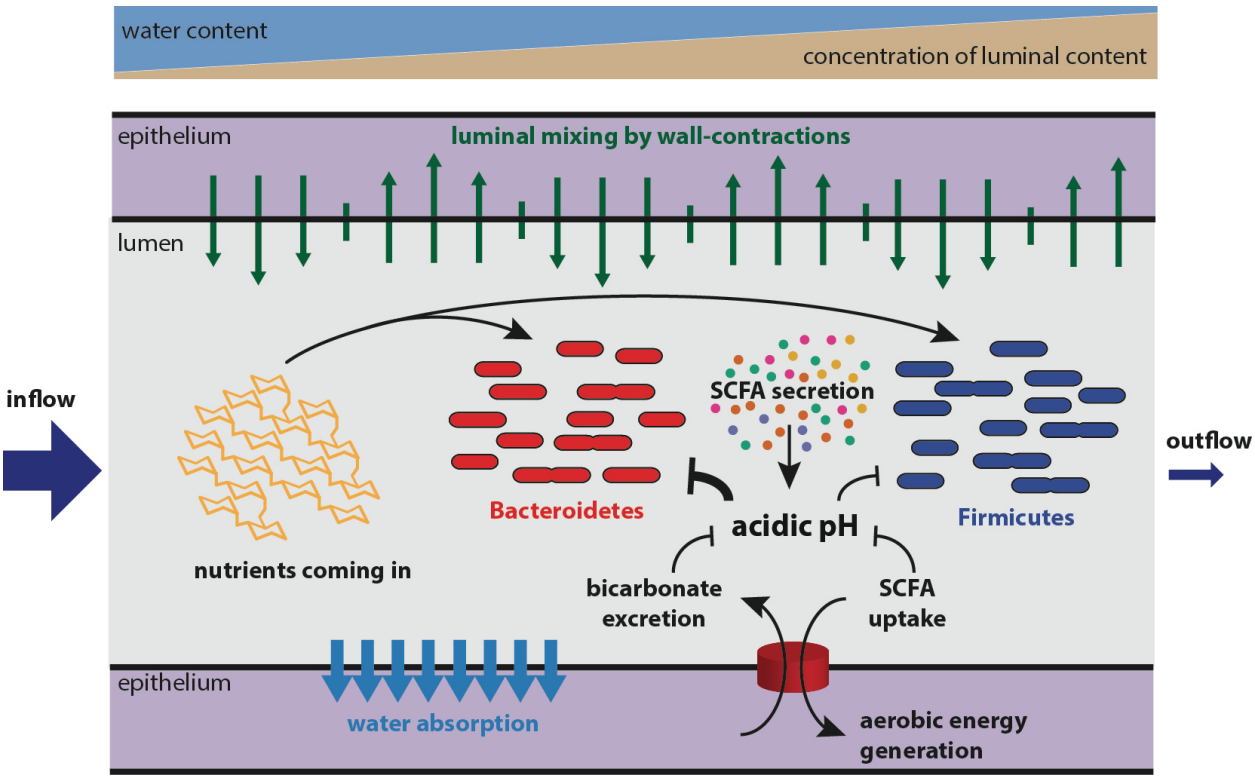

Figure S6. Schematic representation of the components of the model and their interactions. In short, inflow volumes into the colon from the ileum are 15-20 times greater than the volumes that exit it through the rectum (dark blue arrows). This difference is accounted for by water absorption into the epithelium along the length of the colon (light blue arrows). This water absorption leads to a concentration of nutrients, bacteria, SCFA, and bicarbonate in the colonic lumen. Incoming nutrients (yellow, schematic representation of a polysaccharide) are consumed by bacteria (red for Bacteroidetes, blue for Firmicutes), which ferment the nutrients to produce SCFA (colored points). These SCFA lower the local pH, which in turn inhibits bacterial growth, with a stronger effect on Bacteroidetes than on Firmicutes. The colonic epithelium imports SCFA and excretes bicarbonate. This counteracts the acidification of luminal pH by bacterial SCFA secretion.

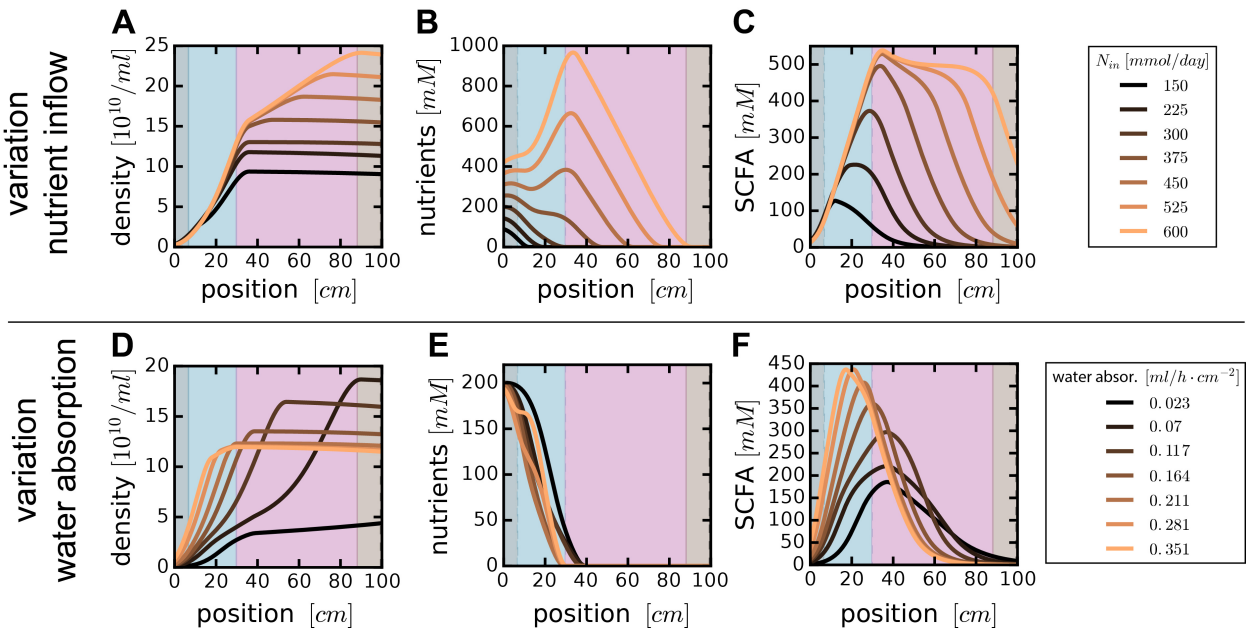

Figure S7. Spatial profiles of different variables for different values of nutrient influx and water-absorption. (A-C) For changes in nutrient influx (colored legend) emerging profiles of (A) total bacterial density, (B) nutrient concentration, and (C) total SCFA concentration are shown. (D-F) For changes in water absorption (colored legend) emerging profiles of (D) total bacterial density, (E) nutrient concentration, and (F) total SCFA concentration. Other parameters are the same as in Figures 3 and 4 (for changes in nutrient influx), and Figure 5 (for changes in water absorption). Full parameter list in Tables S1, S2.

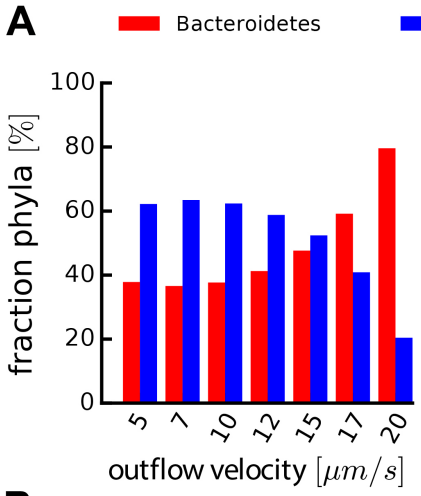

outflow $[\mu m/s]$	transit time $[h]$	BSS
5.0	92	2
7.5	63	3
10.0	48	4
12.5	39	4
15.0	33	5
17.5	29	5
20.0	25	5

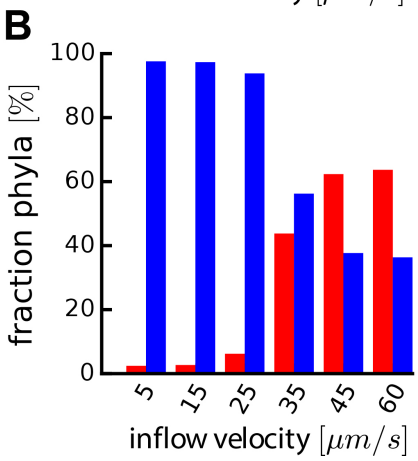

inflow $[\mu m/s]$	transit time $[h]$	BSS
5.0	105	1
15.0	101	1
25.0	96	1
35.0	90	2
45.0	83	2
60.0	73	3

Figure S8. The effect of inflow and outflow on microbiota composition. Changes in flow-velocity by changes in rates of inflow and outflow rate. (A) Relative abundances of Bacteroidetes and Firmicutes in the distal colon for different values of outflow velocity. (B) Relative abundances for different values of inflow-velocity. Table shows relation of water absorption to colonic transit times (TT) and stool consistency (BSS); see SI 5.8 for details of relation. Parameters as in Figures 3 and 5. Water absorption here is reference value, $0.25\,\frac{ml}{h\,cm^2}$. In (A), inflow velocity $v_{in} = 32\,\frac{\mu m}{s}$ $(1.5\,\frac{l}{day})$. In (B), outflow velocity $v_{out} = 5\,\frac{\mu m}{s}$ $(0.1\,\frac{l}{day})$. See also Tables S1, S2 for parameter list. Values for position $x = 1m$ (proximal colon). 120 hours simulation time.

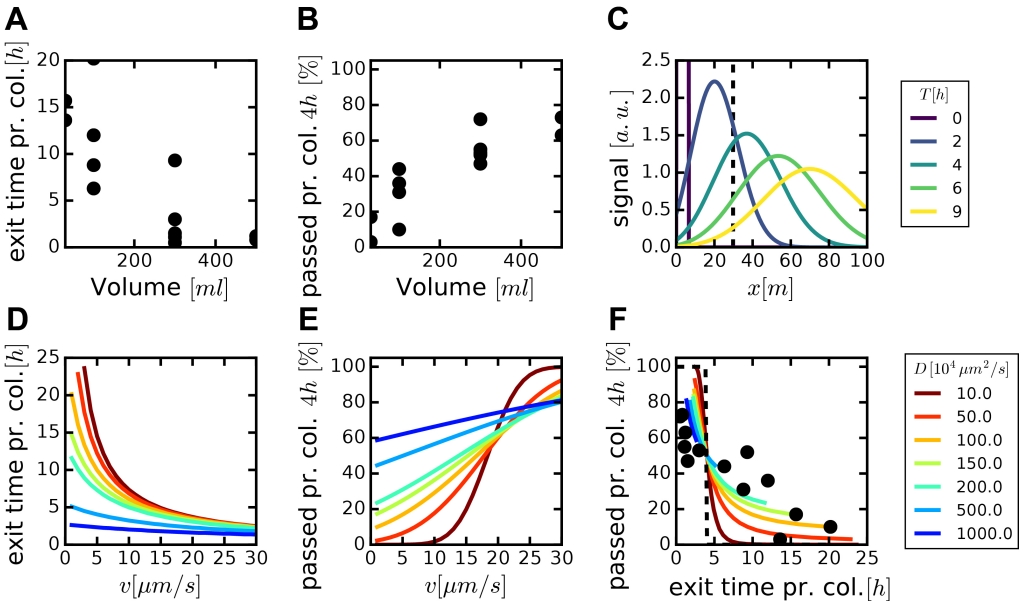

Figure S9. Quantification of the strength of hydrodynamic mixing in the human proximal colon. (A and B) Observations from Hammer and Phillips (23) for different infused volumes: (A) mean exit time from the proximal colon (B) fraction of signal that has passed the proximal colon after 4 hours, as derived by Hammer and Phillips from tracking of radiolabeled particles. (C)-(E) Simulation of marker-spread dynamics by a convection-diffusion equation to estimate mixing dynamics by an effective diffusion process, as confirmed by a controlled in-vitro setup (5) (see SI 2.4 for details). (C) Simulated marker distribution over the length of the colon plotted for different times (colored legend) . Dashed line denotes end of proximal colon. (D) and (E) mean exit time from the proximal colon and fraction of signal that has passed the proximal colon after four hours, as derived from simulations. Differently colored lines denote different mixing strength (see legend). (F) Comparison of simulations (lines) with observations by Hammer and Phillips (dots). Parameters are $v = 20\mu m/s$ in (C,F) and $D = 100\mu m^2/s$ in (C). See SI 2.4 for details.

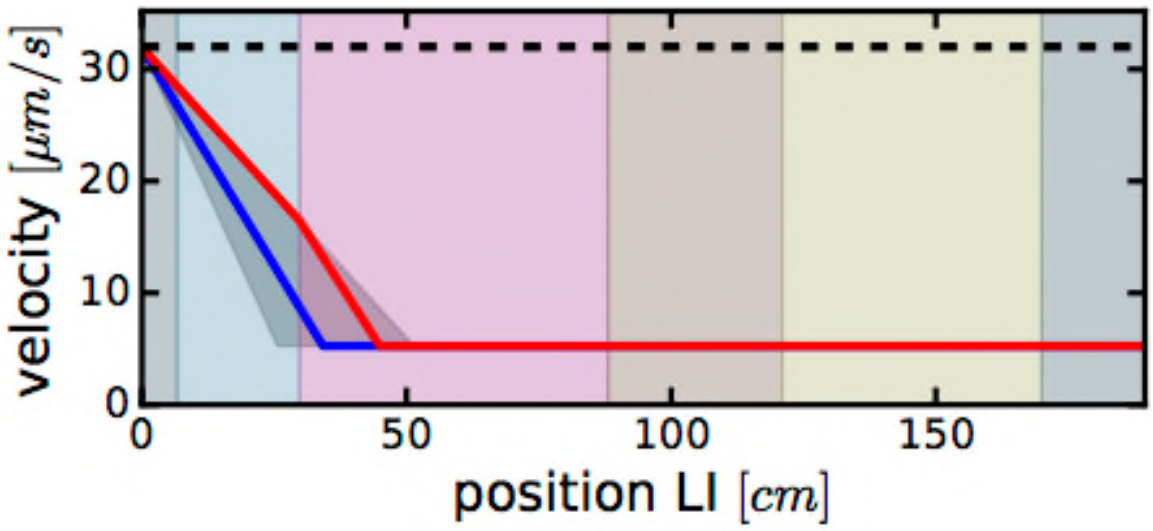

Figure S10. Flow-velocities in the colon. Red line indicates upper boundary of mean flow-velocity based on homogenous absorption along the colon. Blue line shows used flow-velocity profile. See SI 2.2 for details.

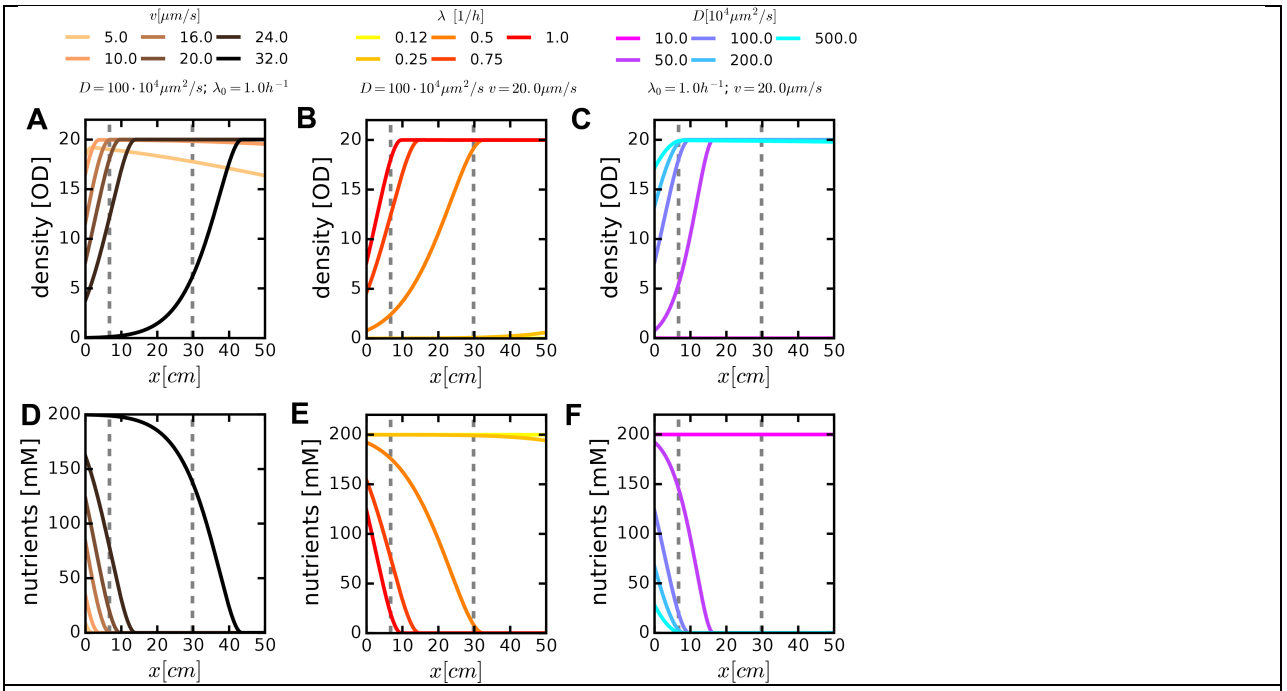

Figure S11. Simulation of bacterial growth and nutrient levels under flow and mixing without flow gradients. Illustration of bacterial density and nutrient abundance for the first 50cm of the colon when no water-absorption is present. Dynamics shown for different inflow-velocity v (left coloumn), growth-rate λ (center column) and mixing D (right column). (A-C) Change of bacterial density along first 50cm of colon. (D-F) Change of nutrient concentration along first 50cm of colon. Values for parameters v, D, λ are indicated in panels.

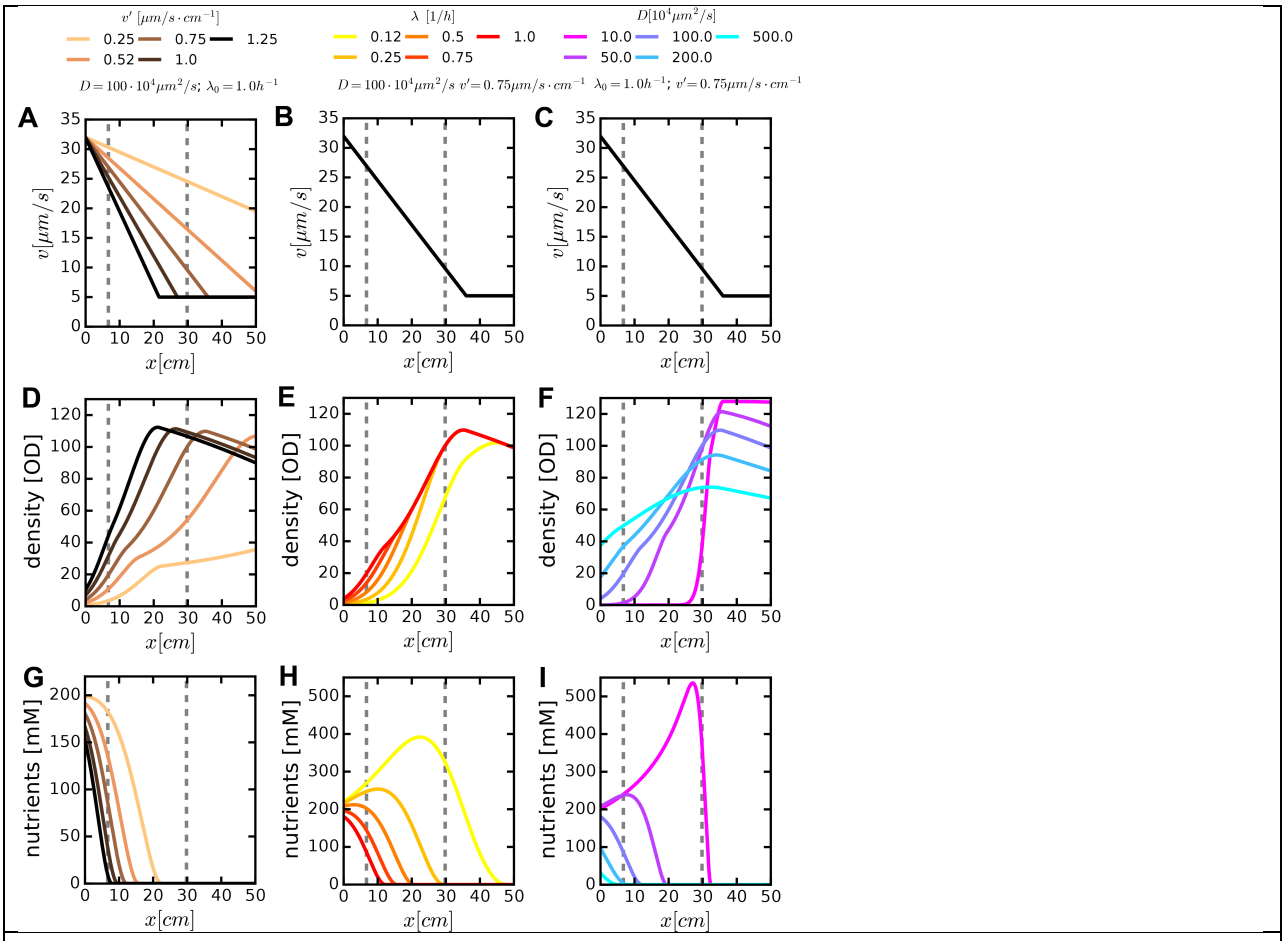

Figure S12. Simulation of bacterial growth and nutrient levels under flow and mixing with flow velocity gradients. Shown are spatial profiles along the first 50cm of the colon and changed water-absorption rate v', growth-rate λ_0, and mixing D. (A-C) Illustration of flow velocities. (C-F) Bacterial. (G-I) Nutrient concentrations. Values for parameters v, D, λ are indicated in panels.

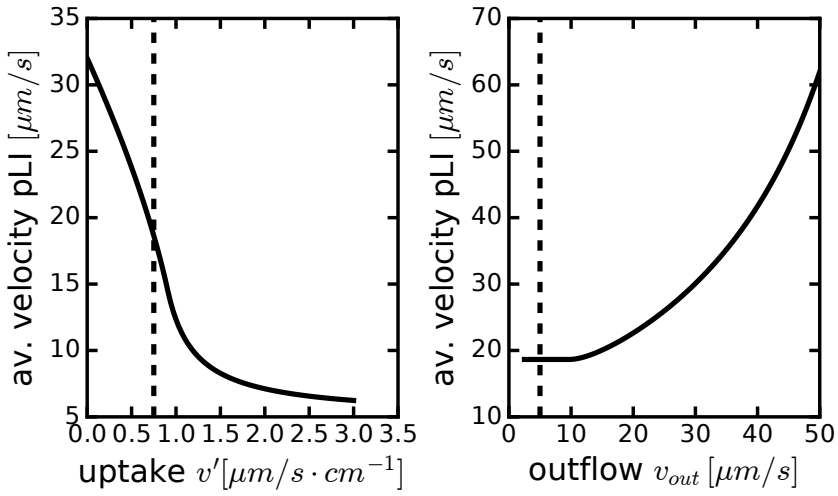

Figs S13. Average velocity in the proximal large intestine. (A) Dependence on water-absorption. (B) Dependence on outflow velocity. See SI 2.2 for details of used flow profile.

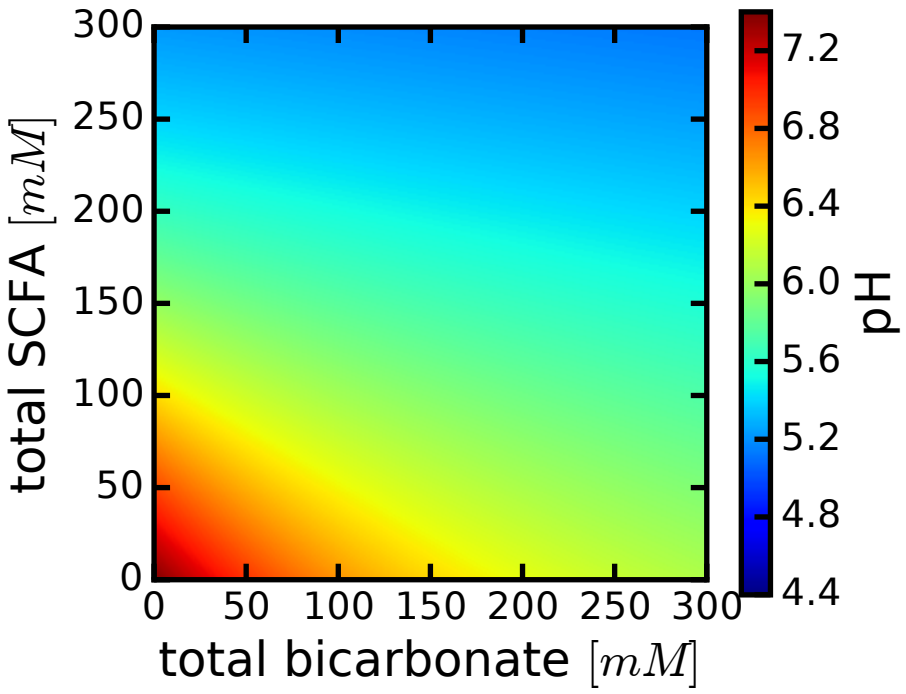

Figure S14: pH in the lumen, depending on total bicarbonate and SCFA concentration. Values followed by including measured buffer behavior of the lumen. Details are described in SI 4.

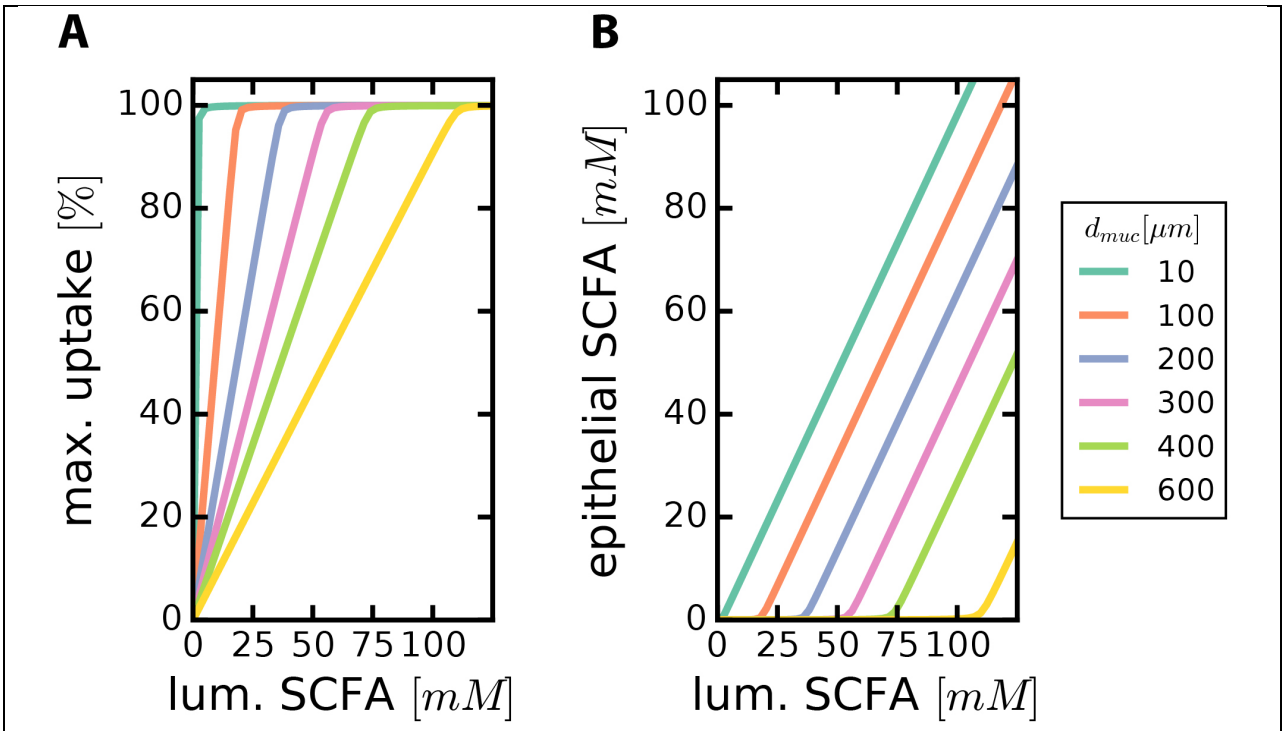

Figure S15. Uptake of SCFA through the mucus layer. Uptake rate of SCFA depends on luminal SCFA concentration. (A) Uptake rate depending on SCFA concentration in lumen. (B) SCFA concentration at epithelial layer depending on SCFA concentration in lumen. For estimated mucus thickness (about $400\mu m$), uptake rate falls to about 50% at 20mM. This is approximately the concentration of different SCFA in the distal colon. See SI 5.4 for details.

Supplementary References

1. Holdeman LV, Cato EP, Moore W (1977) Anaerobic Laboratory Manual. 1–140.

2. R Development Core Team (2010) *R: A language and environment for statistical computing.* (R Foundation for Statistical Computing, Vienna, Austria) Available at: http://www.R-project.org.

3. Morhac M (2012) *Peaks: Peaks* (R package version 0.2).

4. Monod J (1949) The Growth of Bacterial Cultures. *Annu Rev Microbiol* 3(1):371–394.

5. Cremer J, et al. (2016) Effect of flow and peristaltic mixing on bacterial growth in a gut-like channel. *Proc Natl Acad Sci USA*:201601306.

6. Billich CO, Levitan R (1969) Effects of sodium concentration and osmolality on water and electrolyte absorption form the intact human colon. *J Clin Invest* 48(7):1336–1347.

7. Hounnou G, Destrieux C, Desmé J, Bertrand P, Velut S (2002) Anatomical study of the length of the human intestine. *Surg Radiol Anat* 24(5):290–294.

8. Saunders BP, Phillips RK, Williams CB (1995) Intraoperative measurement of colonic anatomy and attachments with relevance to colonoscopy. *Br J Surg* 82(11):1491–1493.

9. Khashab M, Pickhardt P, Kim D, Rex D (2009) Colorectal anatomy in adults at computed tomography colonography: normal distribution and the effect of age, sex, and body mass index. *Endoscopy* 41(08):674–678.

10. Sadahiro S, Ohmura T, Yamada Y, Saito T, Taki Y (1992) Analysis of length and surface area of each segment of the large intestine according to age, sex and physique. *Surg Radiol Anat* 14(3):251–257.

11. Pritchard SE, et al. (2014) Fasting and postprandial volumes of the undisturbed colon: normal values and changes in diarrhea-predominant irritable bowel syndrome measured using serial MRI. *Neurogastroenterol Motil* 26(1):124–130.

12. Devroede GJ, Phillips SF (1969) Studies of the perfusion technique for colonic absorption. *Gastroenterology*.

13. Debongnie JC, Phillips SF (1978) Capacity of the human colon to absorb fluid. *Gastroenterology* 74(4):698–703.

14. Phillips SF, Giller J (1973) The contribution of the colon to electrolyte and water conservation in man. *J Lab Clin Med* 81(5):733–746.

15. Cummings JH, et al. (1978) Colonic response to dietary fibre from carrot, cabbage, apple, bran, and guar gum. *Lancet* 1(8054):5–9.

16. Stephen AM, Cummings JH (1980) The microbial contribution to human faecal mass. *J Med*

Microbiol 13(1):45–56.

17. Levitan R, Fordtran JS, Burrows BA, Ingelfinger FJ (1962) Water and salt absorption in the human colon. *J Clin Invest* 41:1754–1759.

18. Sandle GI (1998) Salt and water absorption in the human colon: a modern appraisal. *Gut*.

19. Devroede GJ, Phillips SF, Code CF, Lind JF (1971) Regional differences in rates of insorption of sodium and water from the human large intestine. *Can J Physiol Pharmacol* 49(12):1023–1029.

20. Devroede GJ, Phillips SF (1970) Failure of the human rectum to absorb electrolytes and water. *Gut* 11(5):438–442.

21. Proano M, et al. (1991) Unprepared human colon does not discriminate between solids and liquids. *Am J Physiol* 260(1 Pt 1):G13–6.

22. Cummings JH, Jenkins DJ, Wiggins HS (1976) Measurement of the mean transit time of dietary residue through the human gut. *Gut* 17(3):210–218.

23. Hammer J, Phillips SF (1993) Fluid loading of the human colon: effects on segmental transit and stool composition. *Gastroenterology* 105(4):988–998.

24. Gorbach SL, et al. (1967) Studies of intestinal microflora. II. Microorganisms of the small intestine and their relations to oral and fecal flora. *Gastroenterology* 53(6):856–867.

25. Marteau P, et al. (2001) Comparative Study of Bacterial Groups within the Human Cecal and Fecal Microbiota. *Appl Environ Microbiol* 67(10):4939–4942.

26. Mahowald MA, et al. (2009) Characterizing a model human gut microbiota composed of members of its two dominant bacterial phyla. *Proc Natl Acad Sci USA* 106(14):5859–5864.

27. Verberkmoes NC, et al. (2008) Shotgun metaproteomics of the human distal gut microbiota. *ISME J* 3(2):179–189.

28. Sonnenburg JL, Angenent LT, Gordon JI (2004) Getting a grip on things: how do communities of bacterial symbionts become established in our intestine? *Nat Immunol* 5(6):569–573.

29. Bäckhed F, Ley RE, Sonnenburg JL, Peterson DA, Gordon JI (2005) Host-bacterial mutualism in the human intestine. *Science* 307(5717):1915–1920.

30. Lee SM, et al. (2013) Bacterial colonization factors control specificity and stability of the gut microbiota. *Nature*:1–6.

31. Johansson MEV, Larsson JMH, Hansson GC (2011) The two mucus layers of colon are organized by the MUC2 mucin, whereas the outer layer is a legislator of host-microbial interactions. *Proc Natl Acad Sci USA* 108(Supplement_1):4659–4665.

32. Zoetendal EG, et al. (2002) Mucosa-Associated Bacteria in the Human Gastrointestinal Tract Are Uniformly Distributed along the Colon and Differ from the Community Recovered from Feces.

Appl Environ Microbiol 68(7):3401–3407.

33. Albenberg L, et al. (2014) Correlation Between Intraluminal Oxygen Gradient and Radial Partitioning of Intestinal Microbiota. *Gastroenterology* 147(5):1055–1063.e8.

34. Espey MG (2013) Free Radical Biology and Medicine. *Free Radical Biology and Medicine* 55(C):130–140.

35. Sarna S (2010) *Colonic Motility* (Morgan & Claypool Publishers).

36. Hardcastle JD, Mann CV (1968) Study of large bowel peristalsis. *Gut* 9(5):512–520.

37. Van Houte J, Gibbons RJ (1966) Studies of the cultivable flora of normal human feces. *Antonie Van Leeuwenhoek* 32(2):212–222.

38. Moore WE, Holdeman LV (1974) Human fecal flora: the normal flora of 20 Japanese-Hawaiians. *Appl Microbiol* 27(5):961–979.

39. McNeil NI (1984) The contribution of the large intestine to energy supplies in man. *Am J Clin Nutr*.

40. Bergman EN (1990) Energy contributions of volatile fatty acids from the gastrointestinal tract in various species. *Physiol Rev* 70(2):567–590.

41. Bingham S, Cummings JH, McNeil NI (1979) Intakes and sources of dietary fiber in the British population. *Am J Clin Nutr* 32(6):1313–1319.

42. Southgate DA, Durnin JV (1970) Calorie conversion factors. An experimental reassessment of the factors used in the calculation of the energy value of human diets. *Br J Nutr* 24(2):517–535.

43. Topping DL, Clifton PM (2001) Short-chain fatty acids and human colonic function: roles of resistant starch and nonstarch polysaccharides. *Physiol Rev* 81(3):1031–1064.

44. Cummings JH (1981) Dietary fibre. *Br Med Bull* 37(1):65–70.

45. Ley RE, Turnbaugh PJ, Klein S, Gordon JI (2006) Microbial ecology: human gut microbes associated with obesity. *Nature* 444(7122):1022–1023.

46. Payne AN, Chassard C, Lacroix C (2012) Gut microbial adaptation to dietary consumption of fructose, artificial sweeteners and sugar alcohols: implications for host-microbe interactions contributing to obesity. *Obes Rev* 13(9):799–809.

47. Suez J, et al. (2014) Artificial sweeteners induce glucose intolerance by altering the gut microbiota. *Nature*:1–17.

48. The Human Microbiome Project Consortium (2013) Structure, function and diversity of the healthy human microbiome. *Nature* 486(7402):207–214.

49. Flint HJ, Bayer EA, Rincon MT, Lamed R, White BA (2008) Polysaccharide utilization by gut bacteria: potential for new insights from genomic analysis. *Nat Rev Micro* 6(2):121–131.

50. Flint HJ, Scott KP, Louis P, Duncan SH (2012) The role of the gut microbiota in nutrition and health. *Nat Rev Gastroentero* 9(10):577–589.

51. Duncan SH, Louis P, Thomson JM, Flint HJ (2009) The role of pH in determining the species composition of the human colonic microbiota. *Environ Microbiol* 11(8):2112–2122.

52. Gaudichon C, et al. (2002) Ileal losses of nitrogen and amino acids in humans and their importance to the assessment of amino acid requirements. *Gastroenterology* 123(1):50–59.

53. Chacko A, Cummings JH (1988) Nitrogen losses from the human small bowel: obligatory losses and the effect of physical form of food. *Gut* 29(6):809–815.

54. Cummings JH, Macfarlane GT (1997) Role of intestinal bacteria in nutrient metabolism. *Clin Nutr* 16:3–11.

55. Macfarlane GT, Gibson GR, Cummings JH (1992) Comparison of fermentation reactions in different regions of the human colon. *J Appl Bacteriol* 72(1):57–64.

56. Maxwell MH, Kleeman CR, Narins RG (1994) *Maxwell & Kleeman's Clinical Disorders of Fluid and Electrolyte Metabolism* (McGraw-Hill Companies).

57. McNeil NI, Cummings JH, James WP (1978) Short chain fatty acid absorption by the human large intestine. *Gut* 19(9):819–822.

58. Besten den G, et al. (2013) The role of short-chain fatty acids in the interplay between diet, gut microbiota, and host energy metabolism. *J Lipid Res* 54(9):2325–2340.

59. Harig JM, Ng EK, Dudeja PK, Brasitus TA, Ramaswamy K (1996) Transport of n-butyrate into human colonic luminal membrane vesicles. *Am J Physiol* 271(3 Pt 1):G415–22.

60. Duncan SH, Flint HJ (2008) Proposal of a neotype strain (A1-86) for Eubacterium rectale. Request for an Opinion. *Int J Syst Evol Micr* 58(7):1735–1736.

61. Endeward V, Gros G (2005) Low carbon dioxide permeability of the apical epithelial membrane of guinea-pig colon. *J Physiol (Lond)* 567(1):253–265.

62. Davenport H (1974) *The ABC of acid-base chemistry* (University of Chicago Press). 6 Ed.

63. Macy JM, Ljungdahl LG, Gottschalk G (1978) Pathway of succinate and propionate formation in Bacteroides fragilis. *J Bacteriol* 134(1):84–91.

64. Macfarlane GT, Gibson GR (1997) Carbohydrate Fermentation, Energy Transduction and Gas Metabolismin the Human Large Intestine. *Gastrointestinal Microbiology*, eds Mackie R, White B, Isaacson RE (Springer Science & Business Media), pp 269–318.

65. Louis P, Flint HJ (2009) Diversity, metabolism and microbial ecology of butyrate-producing bacteria from the human large intestine. *FEMS Microbiol Lett* 294(1):1–8.

66. Rechkemmer G, Rönnau K, Engelhardt von W (1988) Fermentation of polysaccharides and

absorption of short chain fatty acids in the mammalian hindgut. *Comp Biochem Physiol* 90(4):563–568.

67. Henderson LJ (1908) The theory of neutrality regulation in the animal organism. *Am J Physiol* 21(4):427–448.

68. Hasselbalch KA (1916) Die Berechnung der Wasserstoffzahl des Blutes aus der freien und gebundenen Kohlensäure desselben, und die Sauerstoffbindung des Blutes als Funktion der Wasserstoffzahl. *Biochem Z* 78:112–144.

69. Fadda HM, et al. (2010) Drug Solubility in Luminal Fluids from Different Regions of the Small and Large Intestine of Humans. *Mol Pharm* 7(5):1527–1532.

70. Lindahl A, Ungell AL, Knutson L, Lennernäs H (1997) Characterization of fluids from the stomach and proximal jejunum in men and women. *Pharm Res* 14(4):497–502.

71. Persson EM, et al. (2005) The Effects of Food on the Dissolution of Poorly Soluble Drugs in Human and in Model Small Intestinal Fluids. *Pharm Res* 22(12):2141–2151.

72. Evans DF, et al. (1988) Measurement of gastrointestinal pH profiles in normal ambulant human subjects. *Gut* 29(8):1035–1041.

73. Gustafsson JK, et al. (2012) An ex vivo method for studying mucus formation, properties, and thickness in human colonic biopsies and mouse small and large intestinal explants. *Am J Physiol-Gastr L* 302(4):G430–G438.

74. Johansson MEV, et al. (2013) Bacteria penetrate the normally impenetrable inner colon mucus layer in both murine colitis models and patients with ulcerative colitis. *Gut*.

75. Peppas NA, Hansen PJ, Buri PA (1984) A theory of molecular diffusion in the intestinal mucus. *Int J Pharm*.

76. Domalski ES, Hearing ED Condensed Phase Thermochemistry Data. *NIST Chemistry WebBook, NIST Standard Reference Database Number 69*, eds Lindstrom PJ, Mallard WG (National Institute of Standards and Technology, Gaithersburg MD, 20899). Available at: http://webbook.nist.gov.

77. Lewis SJ, Heaton KW (1997) Stool Form Scale as a Useful Guide to Intestinal Transit Time. *Scand J Gastroenterol* 32(9):920–924.

78. Degen LP, Phillips SF (1996) How well does stool form reflect colonic transit? *Gut* 39(1):109–113.

79. O'Donnell LJ, Virjee J, Heaton KW (1990) Detection of pseudodiarrhoea by simple clinical assessment of intestinal transit rate. *BMJ* 300(6722):439–440.

80. Guyer JE, Wheeler D, Warren JA (2009) FiPy: partial differential equations with python. *Comput Sci Eng*.

81. Cummings JH, Englyst HN (1987) Fermentation in the human large intestine and the available substrates. *Am J Clin Nutr* 45(5 Suppl):1243–1255.

82. Kleessen B, Sykura B, Zunft HJ, Blaut M (1997) Effects of inulin and lactose on fecal microflora, microbial activity, and bowel habit in elderly constipated persons. *Am J Clin Nutr* 65(5):1397–1402.